# The Effect of Boron Nitride Flakes on Na Ion Transport in PEO Electrolytes

Shreyas Pathreeker<sup>1</sup>, Colby A. Snyder<sup>1</sup>, George V. Papamokos<sup>2</sup>, Prof. Russell J. Composto\*, 1, 3

<sup>1</sup>Department of Materials Science and Engineering, University of Pennsylvania, Philadelphia, PA, United States

<sup>2</sup> School of Engineering and Applied Sciences, Harvard University, Cambridge, MA, United States <sup>3</sup>Department of Chemical and Biomolecular Engineering, University of Pennsylvania, Philadelphia, PA, United States

\*Corresponding author: <a href="mailto:composto@seas.upenn.edu">composto@seas.upenn.edu</a>

#### Abstract

Improving the total ionic conductivity ( $\sigma$ ) of solid polymer electrolytes (SPEs) is critical to the development of solid-state sodium (Na) batteries. In this work, we investigate the effect of twodimensional (2D), dual-Lewis hexagonal boron nitride (h-BN) filler on polymer structure and ion transport properties of P(EO)<sub>24</sub>:Na<sup>+</sup> and P(EO)<sub>4</sub>:Na<sup>+</sup> mixtures of poly (ethylene oxide) (PEO)–bis (fluorosulfonylimide) (NaFSI). Below the critical percolation concentration threshold for the h-BN flakes, x-ray diffraction (XRD) and differential scanning calorimetry (DSC) studies show that an increase in h-BN concentration initially induces an increase in PEO crystallinity followed by a decrease due to competing effects between heterogeneous nucleation of PEO lamellae and its spherulitic confinement, respectively. Raman spectroscopy reveals that h-BN improves NaFSI dissociation in the semi-dilute SPEs which is supported by density functional theory (DFT) calculations. Our calculations suggest that PEO can almost fully dissociate an NaFSI molecule with a coordination number of 6. We propose an h-BN-'assisted' mechanism to explain this observation, wherein h-BN aids PEO in better matching the dissociation energy of the NaFSI salt by virtue of its dual–Lewis surface chemistry. A corresponding 4x increase in  $\sigma$  is observed for the P(EO)<sub>24</sub>:Na<sup>+</sup> SPEs using electrochemical impedance spectroscopy (EIS). The P(EO)<sub>4</sub>:Na<sup>+</sup> SPEs do not show this increase likely due to a significantly different local solvation environment wherein contact ion pairs (CIPs) and aggregates (AGGs) dominate. Our findings highlight the role of filler chemistry in the design and development of composite solid polymer electrolytes for Na batteries.

#### 1. Introduction

Sodium (Na) batteries are poised as suitable alternatives to lithium (Li)—batteries due to the relative abundance of Na, its electrochemical equivalence to Li, and the potential cost benefits that can be realized by optimizing cell engineering and design. 1-5 Liquid electrolytes for batteries use flammable solvents, which presents a fire hazard in alkali metal batteries (i.e., where the anode is the native metal itself) wherein the primary failure mechanism of dendrite formation and propagation can lead to internal short-circuit and thermal runaway.<sup>6</sup> This safety risk has necessitated the development of all solid-state batteries wherein the liquid electrolyte is replaced by a solid polymer electrolyte (SPE). Extensive research on SPEs has established that while the high modulus of SPEs makes them safer than their liquid counterparts, dry SPEs are unable to match liquid electrolyte ionic conductivity ( $\sigma$ ) because ionic motion in dry SPEs is cooperative with polymer segmental motion.<sup>7–12</sup> One way to address this challenge is to use Lewis–active filler materials which can modulate intercomponent interactions and improve charge carrier concentration within the SPEs. Further, key polymer properties such as its glass transition temperature  $T_g$  and crystallinity  $X_c$  are directly impacted by filler size, filler geometry, and filler polymer interactions which together govern  $\sigma$ . These complex interactions make composite SPEs an interesting subclass of materials both fundamentally as well as for energy storage applications.

Two-dimensional hexagonal boron nitride (2D h–BN) possesses a dual–Lewis surface chemistry wherein boron behaves as a Lewis acid (electron acceptor), and nitrogen behaves as a Lewis base (electron donor). <sup>13</sup> In addition to this unique chemistry, h–BN has a high thermal conductivity <sup>14</sup> which can be beneficial for SPE thermal and mechanical properties. h–BN has attracted widespread interest for Li–based SPEs, <sup>15, 16</sup> which motivated us to explore its use for Na–based SPEs. At present, there are only a few reports <sup>17–22</sup> on the use of boron in Na–ion batteries. The most common strategy to use boron in polymer electrolytes thus far has been to synthetically incorporate boron atoms into the polymer backbone. Chen et al. <sup>17, 18</sup> have investigated the electrochemical properties of gel polymer electrolytes (GPEs) made of boron–containing polymer matrices polymerized *in–situ*. In one case, <sup>17</sup> they found a marginal decrease in  $\sigma$  of their B–containing electrolytes relative to full–carbon polymer matrices whereas in another they observed the opposite. <sup>18</sup> In both cases, an increased cation transference number was observed due to the ability of boron to trap anions. Genier and co–workers <sup>19</sup> reported similar findings as well as higher  $\sigma$  due to boron. The Liu group<sup>20,21</sup> has also developed and investigated Na–ion batteries comprising

boron–containing GPEs. In an innovative approach, they crosslinked poly(ethylene glycol) PEG–functionalized BN nanosheets into PEG–(diacrylate)DA gel networks and observed a marginal increase in  $\sigma$  and good cycling behavior compared to identical BN–free systems. More recently, the same group reported a boron–covalent organic framework (B–COF)–based polymer electrolyte with excellent electrochemical properties. Collectively, the chemistry–heavy nature of such approaches can be a hindrance, and it remains unclear as to how the dual–Lewis chemistry of h–BN (as opposed to boron alone) affects sodium ion transport in SPEs. Conversely, the simple dispersion of h–BN filler in a polymer matrix has received little attention for sodium SPEs.

Our group recently reported on structure–property relationships in PEO/NaNO<sub>3</sub>/h–BN SPEs.<sup>22</sup> We found a non–monotonic change in PEO crystallinity with increasing h–BN concentration and corresponding changes in  $\sigma$ . Our DFT calculations in that study also revealed the dual–Lewis nature of h–BN. Although NaNO<sub>3</sub> was chosen as a model salt due to its low cost and ease of availability, it is typically not used for battery studies. It is well–known that the lattice energy of the salt is central to its dissociation in polar polymer matrices, <sup>7, 8, 23</sup> and lattice energy depends upon anion chemistry. Building on our previous work, here we investigate PEO/NaFSI/h–BN SPEs. The NaFSI salt possesses a low lattice energy and delocalized charge on the anion which collectively enhance its dissolution in a polymer matrix. Recent computational and experimental work also point towards the electrochemical superiority of NaFSI.<sup>24–26</sup> We use PEO as the model polymer matrix due to its excellent processability, low glass transition temperature ( $T_g$ ),<sup>27</sup> and high dielectric constant.<sup>28–31</sup> The advantage of this polymer–salt combination is good salt dissociation in the PEO matrix, which allows us to focus on elucidating effect of h–BN on the SPEs.

Using a combination of experimental and computational (DFT) methods, we investigate how h–BN affects polymer properties, ion dissociation, and  $\sigma$  in these solvent–free SPEs. This is the first such report on dry PEO/NaFSI/h–BN SPEs to the best of our knowledge. Our XRD and DSC results reveal a non–monotonicity in PEO crystallinity with h–BN loading, similar to our previous findings in NaNO<sub>3</sub>–containing SPEs. However, the local solvate structures using NaFSI are vastly different from those using NaNO<sub>3</sub>. Raman spectroscopy results indicate additional differences in solvation environments between the two salt concentrations explored, and that adding h–BN leads to an increase in the percentage of free charge carriers in the SPEs. Given the complex cation solvation environments in these SPEs, we extend our DFT calculations to capture

PEO-NaFSI-h-BN complexes in addition to fully-dissociated, isolated ions. Our DFT calculations reveal that in a 6-fold coordination, PEO can match the ionic interaction energy between Na and FSI thereby dissociating it. EIS measurements of the h-BN-containing SPEs reveal that the addition of h-BN leads to a 2x-4x improvement in  $\sigma$  relative to h-BN-free SPEs. Based on a thorough analysis of the underlying transport parameters using empirically-derived equations, and our DFT results, we present a molecular picture of the driving force behind this improvement. These performance enhancements are more pronounced at the lower salt concentration than at the higher salt concentration explored, which we attribute to differences in the local solvate structure and salt-to-filler ratio. Notably, this simple dispersion technique using 2D h-BN yields  $\sigma$  values on the order of 0.35 mS/cm at 65°C, attributed to the dual-Lewis chemistry of h-BN.

## 2. Materials and Methods

## 2.1 Materials

Poly (ethylene oxide) (PEO, MW 35 kDa) was purchased from Sigma–Aldrich, Inc., and sodium bisfluorosulfonylimide (NaFSI, 99.9%) was purchased from Solvionic, France. The salt was stored in an argon environment due to its hygroscopic nature. Hexagonal boron nitride flakes (h–BN, approximately 5 μm wide and 80 nm thick) were purchased from US Research Nanomaterials and used as received.

## 2.2 Sample preparation

First, PEO polymer was dissolved in acetonitrile in a weight ratio of 0.67:1 PEO:acetonitrile followed by the addition of h–BN flakes to the polymer solution(s). Next, NaFSI salt was dissolved in these mixtures to obtain EO:Na<sup>+</sup> (etheric oxygen of PEO to sodium cation) molar ratios of 24:1 and 4:1. Two h–BN weight loadings were explored for each salt concentration: 0.3 wt.% and 3 wt.% with respect to the weight of PEO in the mixtures. Identical mixtures without the h–BN flakes were prepared as controls. All mixtures were prepared inside an argon–filled glovebox. After weighing, the mixtures were stirred at 40°C under ambient conditions for one hour and then sonicated for ten minutes to ensure uniform dispersion of the h–BN flakes. Samples were prepared in pairs. For structural characterization, 80 μL of the polymer electrolyte mixture was pipetted onto a clean substrate (either glass or polished stainless–steel (SS)) approximately 3.14 cm<sup>2</sup> in area, and the solution was spread with a 381–μm–thick doctor blade. Samples for EIS

measurements were prepared identically using SS electrodes affixed with 100 μm quartz spacers secured by Kapton tape. To evaporate the solvent, the samples were heated to 120°C on a hot plate for one hour and then thoroughly dried in a vacuum oven, also at 120°C, for 16 hours. At this stage, all samples were in the melt. The samples were then transferred to a room temperature (22°C) vacuum chamber, where they were cooled at approximately 5°C/minute for at least one hour. For EIS measurements, a second SS electrode (0.785 cm² in area) was placed on top of the spacers, compressing each sample to a uniform thickness of 100 μm.

#### 2.3 Structural characterization

Optical microscopy was carried out in transmission mode using a Leica microscope. X–ray diffraction (XRD) on the SPE films was carried out using a Rigaku MiniFlex diffractometer with Cu–Kα radiation. Fourier transform infrared spectroscopy (FTIR) was carried out on a JASCO X6 spectrometer in attenuated total reflectance (ATR) mode using a resolution of 4 cm<sup>-1</sup>. Differential scanning calorimetry (DSC) was carried out using a TA Instruments Q200 instrument at a heating rate of 10°C/minute. Raman spectroscopy was carried out on a JASCO NRS–5500 instrument equipped with a 532 nm laser source.

## 2.4 Electrochemical impedance spectroscopy

Electrochemical impedance spectroscopy (EIS) measurements on the SPE films were carried out using a Solartron ModuLab XM instrument with an applied AC voltage of 10 mV in a frequency range of 1 MHz to 0.1 Hz. Spectra were collected under vacuum at temperatures ranging from 298 K to 358 K in 10 K intervals. A 20-minute equilibration period was applied at each temperature before collecting the spectrum. The ionic conductivity was determined using the equation:

$$\sigma = \frac{H}{Z \times A}$$

Where H is the thickness of the SPE films, A is their contact surface area with the electrode, and Z is the real impedance extracted from Bode plots.

## 2.5 Density functional theory (DFT) calculations

Quantum-mechanical (QM) calculations were applied to calculate the complexation energy of the [h-BN/Na<sup>+</sup>], [h-BN/FSI<sup>-</sup>], dimethoxyethane (DME)/Na<sup>+</sup> and DME<sub>2</sub>/Na<sup>+</sup> pairs (DME is

representative of the etheric oxygen of PEO). A  $B_{12}N_{12}H_{12}$  molecule, following the formula  $B_{3n}^2N_{3n}^2H_{6n}$  (n = 2) adopted by Wu et al.<sup>34</sup> was used to simulate the h–BN surface. The basis set superposition error (BSSE) was corrected by applying the counterpoise method.<sup>35</sup> The DFT– $\omega B_{97}X$ –D/aug–cc–pVDZ<sup>36, 37</sup> level of theory and basis set were employed. Gaussian16 was used for all calculations reported in this work.

## 3. Results and Discussion

## 3.1 Analysis of Filler Dispersion and Polymer Spherulitic Domains

Dispersion of filler in polymer composites is critical to composite properties.  $^{36-38}$  Further, the size of the characteristic Maltese–cross patterns observed in semicrystalline polymers  $^{22, 39}$  is a good qualitative indicator of polymer crystallinity. These 100+  $\mu$ m–scale spherulites and the ca. 5- $\mu$ m–sized flakes in our work can both be captured by optical microscopy. To this end, polymer crystallinity and the dispersion of the h–BN flakes in the polymer matrix in our SPEs were investigated using optical microscopy as shown in **Figure 1**.

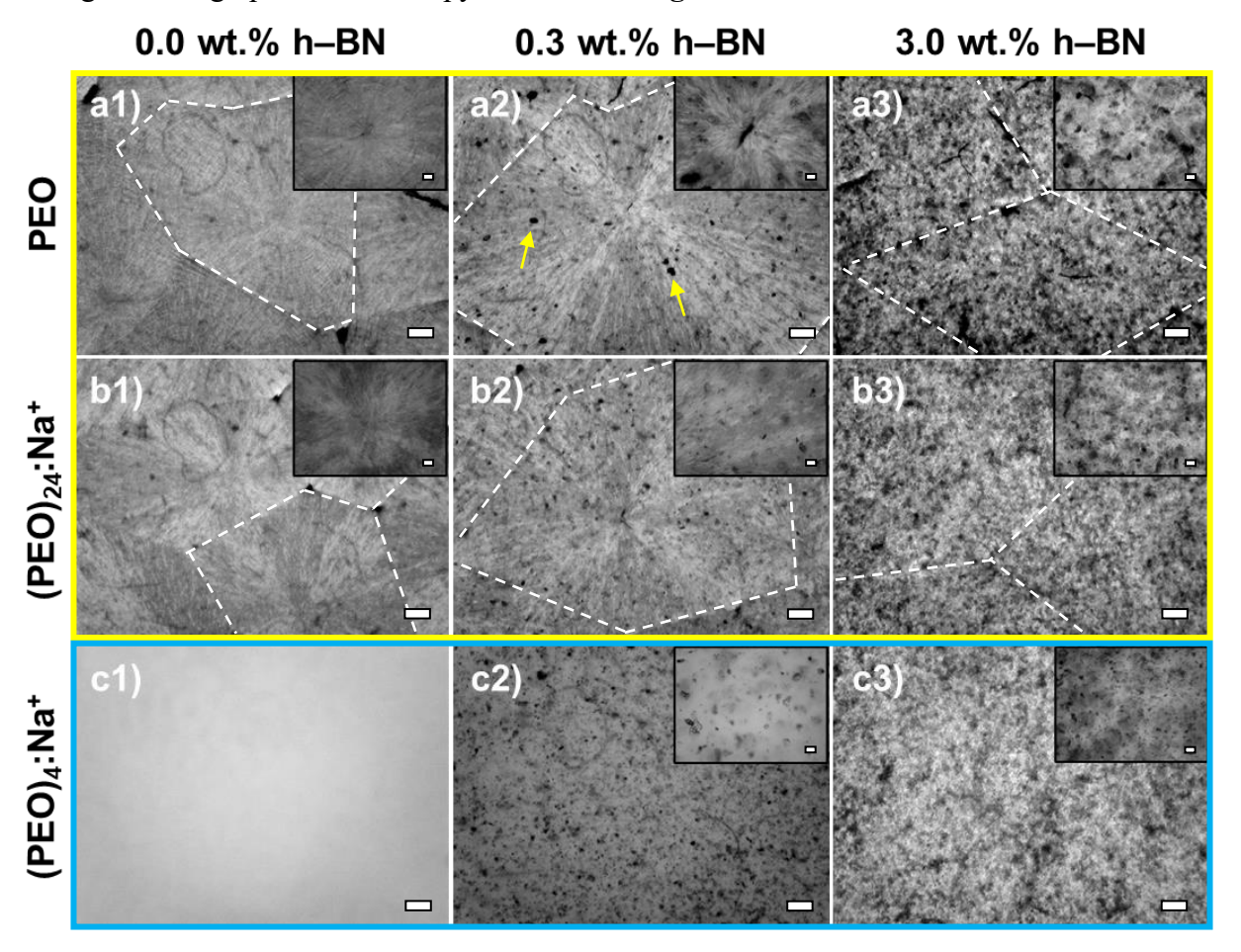


**Figure 1**. Transmission optical micrographs of as—cast SPEs at room temperature. Columns (L–R) represent the concentration of h–BN flakes in the samples, whereas rows (T–B) represent the EO:Na<sup>+</sup> molar ratios. Top row shows salt–free control samples. Yellow box indicates samples that are semicrystalline, and blue box indicates samples that are fully amorphous, at room temperature. Yellow arrows in a2) show stacks of h–BN flakes that appear darker due to greater contrast. Dashed white lines in the top two rows are guides to the eyes demarcating spherulite boundaries in the semicrystalline samples. Main scale bars are 100 μm, and those in the insets are 10 μm.

First, we focus on the effect of salt on the spherulitic morphology (i.e., crystallinity) of PEO. The white dashed lines in Figure 1 demarcate the polymer spherulites for clarity, and the reduction in their size from ca. 700 µm for pure PEO (Figure 1a1)) to ca. 500 µm for the P(EO)<sub>24</sub>:Na<sup>+</sup> sample (Figure 1b1)) is evident, suggesting a reduction in polymer crystallinity with the addition of salt. Further addition of salt, i.e., the P(EO)<sub>4</sub>:Na<sup>+</sup> sample (Figure 1c1)), leads to the complete disappearance of the spherulitic domains of PEO suggesting that the SPEs are fully amorphous at this salt concentration at room temperature. This semicrystalline-to-amorphous phase-transition of PEO is due to polymer-cation complex formation which scales with salt concentration. These findings are in good agreement with previous reports on PEO-based SPEs. 40, <sup>41</sup> Next, we examine the effect of h–BN on PEO crystallinity. It appears that the spherulite size for neat PEO increases from ca. 700 μm (Figure 1a1) to ca. 1000 μm with the addition of 0.3 wt.% h-BN flakes (Figure 1a2)), and shrinks to about 800 µm when h–BN loading is increased to 3.0 wt.% (Figure 1a3)). A similar trend is observed for the P(EO)<sub>24</sub>:Na<sup>+</sup> samples. Qualitatively, this trend suggests that polymer crystallinity increases upon the addition of 0.3 wt.% h-BN, and then decreases when the h-BN concentration is increased to 3.0 wt.%. This trend is in agreement with our previous report on identical SPEs but with NaNO3 salt instead, attributed to the competing effects of surface–enhanced nucleation and spherulitic disruption caused by the h–BN flakes.<sup>22</sup> The P(EO)<sub>4</sub>:Na<sup>+</sup> samples remain fully amorphous with the addition of h–BN.

Next, we turn our attention to the dispersion of h–BN flakes in the polymer (electrolyte) matrices. The optical micrographs consist of light gray areas which represent the polymer matrix, and darker speckles which represent the h–BN flakes. Close examination of the micrographs reveals uniform dispersion of the flakes within the polymer matrices, as well as the absence of agglomerates larger than the nominal lateral dimension of an individual h–BN flake (5 μm). While the 2D geometry of the h–BN flakes may lead to their stacking in the z axis, i.e., across film thickness, these optical micrographs suggest good dispersion of the h–BN flakes in the polymer (electrolyte) matrices even at the highest weight loading of 3.0 wt.% h–BN (see for example Figure

1b2), Figure 1c2), and Figure 1c3)). Given this largely uniform dispersion, we expect the effect of h–BN on polymer structure and  $\sigma$  to also be uniform. Note that the critical volume fraction for percolation (or percolation threshold) calculated using percolation theory<sup>42</sup> for such fillers is about 1.88%, and the weight loadings of h–BN used in this study correspond to volume fractions of 0.162% (0.3 wt.%) and 1.62% (3.0 wt.%) both of which are below the calculated percolation threshold.

# 3.2 Polymer Crystallinity

Salt and filler addition directly impact polymer crystallinity as visualized in Figure 1. Here, we used XRD and DSC to further investigate and quantify changes in PEO crystallinity as a function of salt and h–BN concentration, as shown in **Figure 2**.

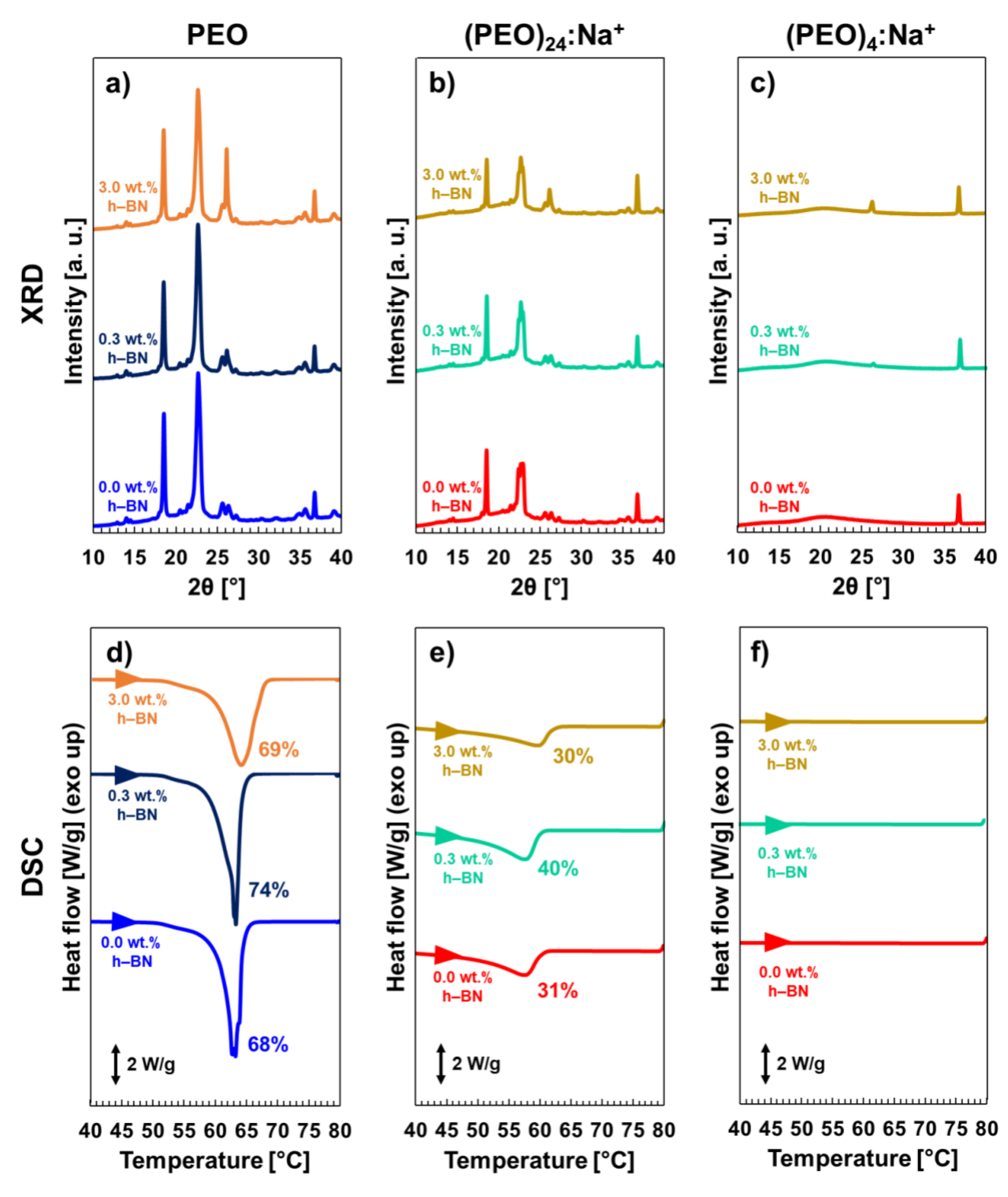


**Figure 2**. Polymer crystallinity characterization. a)—c) XRD traces of the polymer (electrolyte) samples, showing the two main crystalline peaks for PEO located at 19° and 23°. e)—g) DSC heating traces of the polymer (electrolyte) samples showing the melting peak of PEO and PEO–salt complexes. Percent polymer crystallinity is indicated next to the melting peak(s).

Pure PEO exhibits two main crystalline peaks centered at 19° and 23° (Figure 2a)). These peaks correspond to the [120] and the [032] crystal planes of PEO, respectively, <sup>22, 43</sup> and appear at lower absolute intensities for all P(EO)<sub>24</sub>:Na<sup>+</sup> SPEs indicating reduction in PEO crystallinity due to salt addition (Figure 2b)). These two crystalline peaks disappear for all the P(EO)<sub>4</sub>:Na<sup>+</sup> SPEs indicating complete suppression of PEO crystallinity (Figure 2c)). These observations are in excellent agreement with the semicrystalline—to—amorphous phase—transition observed from optical microscopy shown in Figure 1. Although we observed no significant shifts in the PEO peaks upon the addition of salt to PEO, the [032] crystal plane in the P(EO)<sub>24</sub>:Na<sup>+</sup> SPEs appears to reflect as a triplet rather than a single, sharp peak as in pure PEO. Together with the reduction in peak intensities, this observation indicates disruption of the PEO crystal motifs due to the incorporation of salt.

We also quantified the polymer crystallinity in our SPEs using DSC. Table 1 summarizes the key polymer properties for the SPEs. Figure S1 in Supporting Information shows the differential DSC curves used to determine the values of  $T_g$ . As shown in Figure 2d)–Figure 2f), PEO crystallinity decreases from 68% for pure PEO to 31% for P(EO)<sub>24</sub>:Na<sup>+</sup>, and disappears entirely for P(EO)4:Na<sup>+</sup>. Similar behavior is observed for the samples containing h–BN flakes (both 0.3 wt.% and 3.0 wt.%), i.e., PEO crystallinity decreases with increasing salt fraction for all samples investigated (both with and without h-BN flakes). For undoped PEO (Figure 2d)), we find that PEO crystallinity increases from 68% in the absence of h-BN to 74% when 0.3 wt.% h-BN is added. Further increase in h–BN loading to 3.0 wt.% leads to a reduction in PEO crystallinity to ca. 69%. We observe a similar non-monotonic trend for the P(EO)<sub>24</sub>:Na<sup>+</sup> samples, i.e., the SPEs. This trend manifests as a result of the dominance of heterogeneous nucleation at 0.3 wt.% h–BN, versus the dominance of spherulitic confinement at 3.0 wt.% h-BN. The h-BN flakes act as planar surfaces for PEO nucleation and growth, and can catalyze the crystallization of PEO on their surface(s). Thus, PEO crystallinity increases at 0.3 wt.% h–BN. On the other hand, at 3.0 wt.% h– BN the larger number of flakes leads to a smaller inter-particle (i.e., inter-flake) spacing which confines the PEO spherulites and suppresses overall crystallinity. We have observed and reported similar behavior in our previous work on identical SPEs but using NaNO3 as the salt instead of NaFSI.<sup>22</sup> In addition to this, our observations align with other reports in the literature based on polymer and polymer electrolyte composites containing 2D fillers. 44-48

Summarily, our structural characterization reveals uniform dispersion of h–BN flakes within the SPE matrix, and that the P(EO)<sub>24</sub>:Na<sup>+</sup> samples are semicrystalline at room temperature whereas the P(EO)<sub>4</sub>:Na<sup>+</sup> samples are fully amorphous. PEO crystallinity exhibits a non–monotonic trend owing to filler concentration–dependent nucleation and confinement effects. Next, we investigate the solvation structure in our SPEs using Raman spectroscopy.

**Table 1**. Summary of key polymer properties from DSC heating scans for the SPEs. N/A stands for not applicable.

SPE	$T_g$ (°C)	T <sub>m</sub> (°C)	Xc (%)
P(EO) <sub>24</sub> :Na <sup>+</sup> -0.0 wt.% h-BN	-41.5	57.8	31%
P(EO)24:Na <sup>+</sup> -0.3 wt.% h-BN	-41.0	57.9	40%
P(EO)24:Na <sup>+</sup> -3.0 wt.% h-BN	-43.5	59.9	30%
P(EO) <sub>4</sub> :Na <sup>+</sup> -0.0 wt.% h-BN	-40.0	N/A	N/A
P(EO)4:Na <sup>+</sup> -0.3 wt.% h-BN	-41.5	N/A	N/A
P(EO) <sub>4</sub> :Na <sup>+</sup> -3.0 wt.% h-BN	-42.5	N/A	N/A

# 3.3 Solvation Structure and DFT Calculations

Local solvation structure is central to ion transport.<sup>49</sup> We used Raman spectroscopy to analyze the solvation environment within our SPEs, results for which are shown in **Figure 3**. All spectra were collected at room temperature. The characteristic vibrational modes of PEO (800 cm<sup>-1</sup> to 900 cm<sup>-1</sup>) are shown in **Figure S2** in Supporting Information. Pure PEO shows two sharp peaks – one at ca. 845 cm<sup>-1</sup> which represents CH<sub>2</sub> asymmetric rotational modes, and the other at ca. 858 cm<sup>-1</sup> which represents both CH<sub>2</sub> symmetric rotational modes and (C–O–C) symmetric stretching modes.<sup>50</sup> Solvate structures of FSI<sup>-</sup> anion–based salts in various solvents have been studied widely, as recently summarized by Han et al.<sup>51</sup> The deconvoluted data for the S–N–S moiety of the FSI<sup>-</sup> anion (690 cm<sup>-1</sup> to 790 cm<sup>-1</sup>) for both salt concentrations is shown in Figure 3. Incorporation of NaFSI into the PEO matrix results in the formation of a new, broad peak at ca. 720 cm<sup>-1</sup> with a shoulder peak tailing at ca. 740 cm<sup>-1</sup> for all P(EO)<sub>24</sub>:Na<sup>+</sup> SPEs (Figure 3a) to Figure 3c), and **Figure S2**, Supporting Information). There is a corresponding broadening and shift in relative intensities of the PEO peaks which indicates PEO–cation complex formation. However, these peaks still bear resemblance to pure PEO and thus reflect the semicrystalline nature of the P(EO)<sub>24</sub>:Na<sup>+</sup> SPEs as also confirmed in Section 3.2.

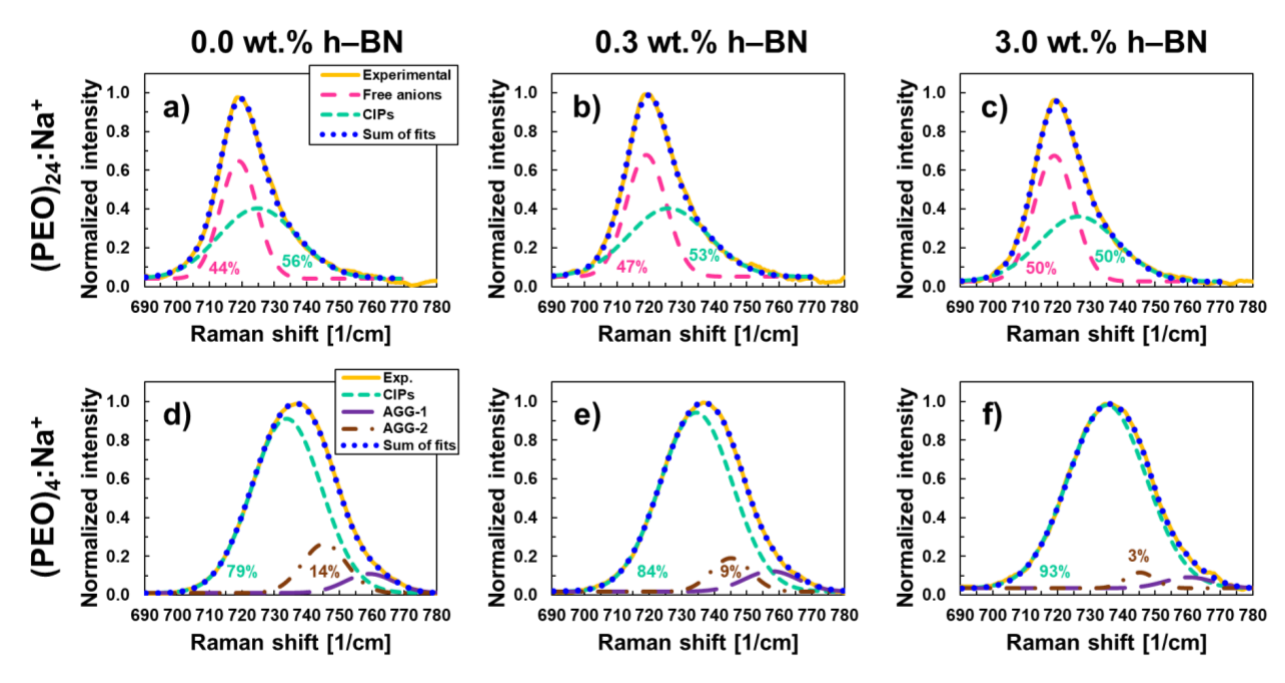


**Figure 3**. Deconvoluted Raman spectra of a)–c) P(EO)<sub>24</sub>:Na<sup>+</sup> SPEs, and d)–f) P(EO)<sub>4</sub>:Na<sup>+</sup> SPEs in the 690 cm<sup>-1</sup> to 780 cm<sup>-1</sup> region capturing the S–N–S vibrational modes from the FSI<sup>-</sup> anion. Columns (L–R) represent 0.0 wt.% h–BN, 0.3 wt.% h–BN, and 3.0 wt.% h–BN. Legend in a) applies to b), c). Legend in d) applies to e), f). Inlaid text indicates the percentage of each species. Purple curves in panels d)–f) are 7% or less in every case.

Increasing the salt concentration from P(EO)<sub>24</sub>:Na<sup>+</sup> to P(EO)<sub>4</sub>:Na<sup>+</sup> results in a large shift of the S–N–S peak shown in Figure 3d)–Figure 3f) from 720 cm<sup>-1</sup> to 737 cm<sup>-1</sup>. On the other hand, the two PEO peaks appear to converge into a single, broad peak upshifted to ca. 863 cm<sup>-1</sup> for all P(EO)<sub>4</sub>:Na<sup>+</sup> SPEs representing the PEO breathing mode characteristic of PEO–cation complexes in accordance with observations made by Ratner and coworkers,<sup>23,52</sup> and more recently by Boschin and Johansson for PEO/NaFSI SPEs at similar salt concentrations.<sup>53</sup>

To elucidate FSI<sup>-</sup> speciation, we follow peak assignments made in the literature for FSI<sup>-</sup>-based electrolytes.<sup>53–58</sup> Results are summarized in **Table 2** and **Table 3**. For the P(EO)<sub>24</sub>:Na<sup>+</sup> SPEs, we deconvoluted our Raman spectra to two peaks: ca. 718 cm<sup>-1</sup> for free anions, and ca. 725 cm<sup>-1</sup> for paired anions. In the absence of h–BN, the percentage of free anions in the P(EO)<sub>24</sub>:Na<sup>+</sup> SPE is ca. 44%, whereas the percentage of contact ion pairs (CIPs) is ca. 56%. Both values are in the vicinity of those reported by Boschin and Johansson for their P(EO)<sub>20</sub>:Na<sup>+</sup> complex at room temperature.<sup>53</sup> Next, we find that the addition of 0.3 wt.% h–BN leads to a gradual increase in the percentage of free anions from 44% to about 50% for the 3.0 wt.% h–BN SPE. We posit that this increase in free anion concentration in the presence of h–BN results from the ability of h–BN to

aid in salt dissociation although there is a concomitant increase in polymer crystallinity by 10% for the 0.3 wt.% h–BN SPE.

**Table 2**. Table summarizing FSI<sup>-</sup> anion speciation for the P(EO)<sub>24</sub>:Na<sup>+</sup> SPEs at room temperature.

SPE	SSIPs	Error	CIPs	Error
P(EO)24:Na <sup>+</sup> -0.0 wt.% h-BN	44%	1.5%	56%	1.7%
P(EO) <sub>24</sub> :Na <sup>+</sup> -0.3 wt.% h-BN	47%	1.8%	53%	2.1%
P(EO)24:Na <sup>+</sup> -3.0 wt.% h-BN	50%	1.5%	50%	1.8%

**Table 3**. Table summarizing FSI<sup>-</sup> anion speciation for the P(EO)<sub>4</sub>:Na<sup>+</sup> SPEs at room temperature.

SPE	CIPs	Error	AGG-1	Error	AGG-2	Error
P(EO) <sub>4</sub> :Na <sup>+</sup> -0.0 wt.% h-BN	79%	3.3%	14%	3.9%	6%	1.2%
P(EO)4:Na <sup>+</sup> -0.3 wt.% h-BN	84%	2.7%	8%	2.9%	7%	1.3%
P(EO)4:Na <sup>+</sup> -3.0 wt.% h-BN	93%	1.7%	3%	0.9%	3%	0.8%

For the P(EO)<sub>4</sub>:Na<sup>+</sup> SPEs, our Raman spectra indicate that the primary peak position is at ca. 737 cm<sup>-1</sup>. Deconvolution of these spectra in a manner similar to that for the P(EO)<sub>24</sub>:Na<sup>+</sup> SPEs did not result in convergence of fits and/or contained large errors. On the other hand, good fits vielded deconvoluted peaks at ca. 733 cm<sup>-1</sup> (CIPs), ca. 745 cm<sup>-1</sup> aggregate species type–1 (AGG– 1), and ca. 758 cm<sup>-1</sup> aggregate species type–2 (AGG–2) which is in accordance with several reports in the literature on MFSI/DME (M = Li, Na) electrolytes. 53-58 The dominant primary Raman peak observed by Boschin and Johannson<sup>53</sup> in their P(EO)<sub>6</sub>:Na<sup>+</sup> SPE (semicrystalline) is centered around 718 cm<sup>-1</sup> indicating the dominance of free anions (ca. 50%), whereas the dominant species in our P(EO)<sub>4</sub>:Na<sup>+</sup> (amorphous) samples appear to be CIPs. This finding highlights the governing role of salt concentration on the solvation environment, and also reflects the sensitivity of the local solvation environment and polymer crystallinity to incremental changes in salt concentration. We find that the addition of h-BN leads to a gradual increase in the percentage of CIPs from 79% to 93% whereas the percentage of both aggregate species (AGG-1 and AGG-2) goes from 20% to 6%. Although deconvolution of this peak is a challenge as also noted by Han and coworkers, 51 it is clear that CIPs dominate the local solvate structure in our P(EO)<sub>4</sub>:Na<sup>+</sup> SPEs. Further, given the breadth of this peak overlapping into the free anion region, we cannot rule out the presence of free

anions at this salt concentration and possibly a corresponding increase in free anion percentage with increase in h–BN concentration.

We also correlated these findings to local PEO coordination (see Figure S3 in Supporting Information). We find that the fraction of coordinated ether oxygen atoms for the P(EO)<sub>24</sub>:Na<sup>+</sup> SPEs increases from 18% to 24% with increased h-BN loading, which indicates that more PEO is partaking in coordination in the presence of h-BN filler. From Figure 3, we know that the percentage of free anions increases in with the addition of h-BN. The corresponding fraction of dissociated cations is expected to coordinate with PEO thereby leading to an increase in the percentage of coordinated ether atoms seen here. Since the 860 cm<sup>-1</sup> region represents both CH<sub>2</sub> and C-O-C modes, the deconvolution leads to relatively large errors. However, this does not prevent us from drawing general conclusions about the trends. For the P(EO)<sub>4</sub>:Na<sup>+</sup> SPEs, the percentage of coordinated PEO appears to go from 95% to 84% when h-BN loading is increased (see Figure S3 in Supporting Information). These values already suggest that coordinated PEO dominates the solvate environment at this salt concentration. The increasing CIP percentage seen in Figure 3 together with the reduction in PEO coordination percentage suggests that although h-BN may aid in salt dissociation, the dissociated ions may recombine if the coordinating moiety on the polymer backbone is saturated. Based on this analysis, we can conclude that the solvation environments in our SPEs are significantly different for the two salt concentrations explored. The P(EO)<sub>24</sub>:Na<sup>+</sup> SPEs consist of free anions (i.e., solvent–separated ion pairs, SSIPs) and CIPs, whereas the P(EO)<sub>4</sub>:Na<sup>+</sup> SPEs consist of CIPs and AGGs. The average coordination number (CN) calculated for the P(EO)<sub>24</sub>:Na<sup>+</sup> SPEs is 4.7±0.3 whereas that for the P(EO)<sub>4</sub>:Na<sup>+</sup> SPEs is 3.5±0.1 which is good agreement with recent molecular dynamics simulations on PEO-NaFSI mixtures at similar concentrations.<sup>59</sup>

To obtain further mechanistic insight into the effect of h–BN on the SPE solvation environment, we carried out DFT calculations to determine the pairwise binding energies of various intercomponent interactions as shown in **Figure 4**. These interactions include NaFSI salt binding, PEO–cation (Na<sup>+</sup>) binding in a systematic incremental coordination number from 2 to 6, and the interaction(s) of h–BN with a fully–dissociated cation and anion as well as with a single PEO unit. Overall, all binding energies are negative, signaling that all pairwise interactions are attractive. We begin with the idea that the complete dissociation of a single NaFSI molecule

requires a minimum binding energy of ca. –108.9 kcal/mol, as shown in Figure 4H. In a mixture of PEO and NaFSI, PEO can form complexes with the Na<sup>+</sup> cation in a variety of coordination numbers (CN) ranging from two to six.

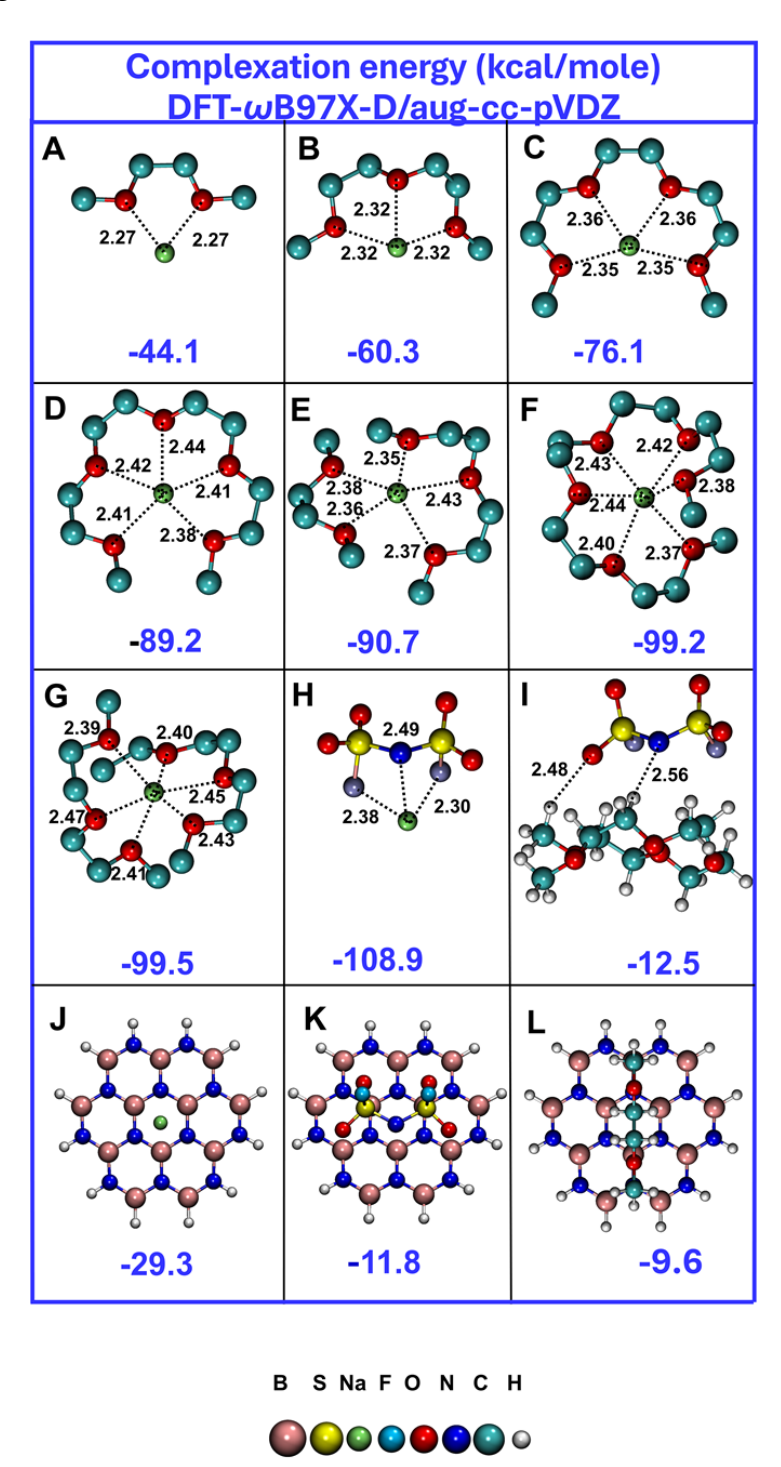


**Figure 4**. Complexation (i.e., binding) energies for various pairwise interactions obtained from DFT calculations: **A, B, C**. PEO-Na<sup>+</sup> interactions with coordination numbers 2, 3, 4, respectively.

**D, E.** PEO-Na<sup>+</sup> interactions with coordination number 5 from one and two PEO chains, respectively. **F, G.** PEO-Na<sup>+</sup> interaction with coordination number 6 from one and two PEO chains, respectively. **H.** NaFSI salt complexation energy. **I.** PEO-FSI<sup>-</sup> interaction (PEO with five ether oxygens). **J.** h-BN-Na<sup>+</sup> pair interaction. **K.** h-BN-FSI<sup>-</sup> pair. **L.** h-BN-PEO-(two ether oxygens).

These complexation energies increase from -44.1 kcal/mol to -99.5 kcal/mol with an increase in the number of coordinating ether oxygen atoms as shown in Figure 4A–G. Next, we find that the FSI<sup>-</sup> anion can bind with PEO with an energy of -12.5 kcal/mol (Figure 4I). The experimentally–derived *CNaverage* for the P(EO)<sub>24</sub>:Na<sup>+</sup> SPEs is around 4.7, and that for the P(EO)<sub>4</sub>:Na<sup>+</sup> SPEs is around 3.5. For comparison, these values agree well with the 4–fold PEO coordination environment reported by Ratner<sup>52</sup> in their foundational work on PEO–NaX complexes. We also find that the *CN* for FSI<sup>-</sup> anions at both salt concentrations is <1. Considering these *CNaverage* values for PEO, our DFT calculations reveal that PEO by itself can offer a binding energy of between -60.1 kcal/mol and -90.0 kcal/mol towards Na<sup>+</sup>, and possibly a small contribution towards FSI<sup>-</sup>. The origin of ion mobility in PEO–NaFSI SPEs lies in this ability of PEO to nearly match the complexation energy of the NaFSI molecule, which has thus far not been shown quantitatively.

Next, we find that h–BN can bind with dissociated Na<sup>+</sup> cations with an energy of –29.3 kcal/mol (Figure 4J) as well as dissociated FSI<sup>-</sup> anions with an energy of –11.8 kcal/mol (Figure 4K) which is similar to the PEO–FSI<sup>-</sup> interaction energy. h–BN can also bind with PEO with an energy of –9.6 kcal/mol (Figure 4L) via hydrogen bonding, which supports our enhanced heterogeneous nucleation theory with regard to PEO crystallinity.

Additionally, we performed DFT calculations for the tricomponent system of PEO–Na<sup>+</sup>–FSI<sup>-</sup> with and without h–BN (see **Figure S4** in Supporting Information). PEO was present with two ether oxygens. We calculated the strength of PEO interaction with NaFSI and the strength of FSI<sup>-</sup> with the Na<sup>+</sup>–PEO complex. We find that the complexation energy of PEO for the NaFSI salt is –31.2 kcal/mol without h–BN, whereas in its presence, it increases to –40 kcal/mol, signifying stronger PEO–salt interactions in the presence of h–BN due to h–BN–salt interactions. For FSI<sup>-</sup>, the interaction energy with the Na<sup>+</sup>–PEO complex is –96 kcal/mole without h–BN and decreases slightly to –95.2 kcal/mol in the presence of h–BN indicating weaker complex–FSI<sup>-</sup> interactions with filler. Although this result indicates the synergistic role of h–BN, the elucidation of the exact

molecular mechanism requires a thorough theoretical study, including periodic DFT calculations and molecular dynamics simulations, which is the subject of a new theoretical study.

Given these findings, the presence of h–BN in the PEO–NaFSI complex can, in principle, match the binding energy required to dissociate NaFSI and lead to a larger fraction of free charge carriers (both Na<sup>+</sup> and FSI<sup>-</sup>) within the SPEs. Notably, our DFT results and analysis support our experimental observations with regard to the percentage of free–charge carriers. Therefore, based on these results, we propose that the general mechanism behind the increased percentage of free charge carriers involves h–BN–'assisted' dissociation of NaFSI salt wherein h–BN and PEO work synergistically to improve salt dissolution in the SPE matrix. The fate of these dissociated charge carriers, however, depends closely upon whether or not the polymer matrix coordinating moiety is saturated. Our finding in this work also agrees with our recent report on h–BN–NO<sub>3</sub><sup>-</sup> binding energy likely due to the higher charge delocalization on the FSI<sup>-</sup> anion. The PEO chains possess much larger configurational entropy than h–BN, which allows PEO to solvate Na<sup>+</sup> cations in multifold configurations easily and facilitate their transport.

In this section, we established using Raman spectroscopy and DFT calculations that the solvation environment in our SPEs depends strongly upon salt concentration. Our  $P(EO)_{24}:Na^+$  SPEs consist primarily of free anions and contact ion pairs, whereas our  $P(EO)_{4}:Na^+$  SPEs comprise mainly contact ion pairs and aggregates. Further, we find that h–BN improves salt dissociation via its ability to bind with both dissociated ions in the SPEs by virtue of its Lewis chemistry. This improvement is also salt–concentration dependent: we see a larger increase at the lower salt concentration, and vice versa which we attribute to the different solvate structures and saturation of PEO. Since  $\sigma$  is proportional to the percentage of free charge carriers, we expect these changes in the solvation environment to reflect in the  $\sigma$  values of our SPEs, which is discussed in the next section.

## 3.4 Ionic Conductivity Analysis

We probed the total ionic conductivity  $\sigma_{DC}$  (referred to hereafter as  $\sigma$ ) of our SPEs using electrochemical impedance spectroscopy (EIS), as shown in **Figure 5**. Impedances were extracted from the frequency-independent portion of Bode plots shown in **Figure S5** and **Figure S6** in

Supporting Information. The EIS data has been scaled to  $1000/(T-T_g)$  so as to account for changes in polymer  $T_g$ , which is sample–specific.

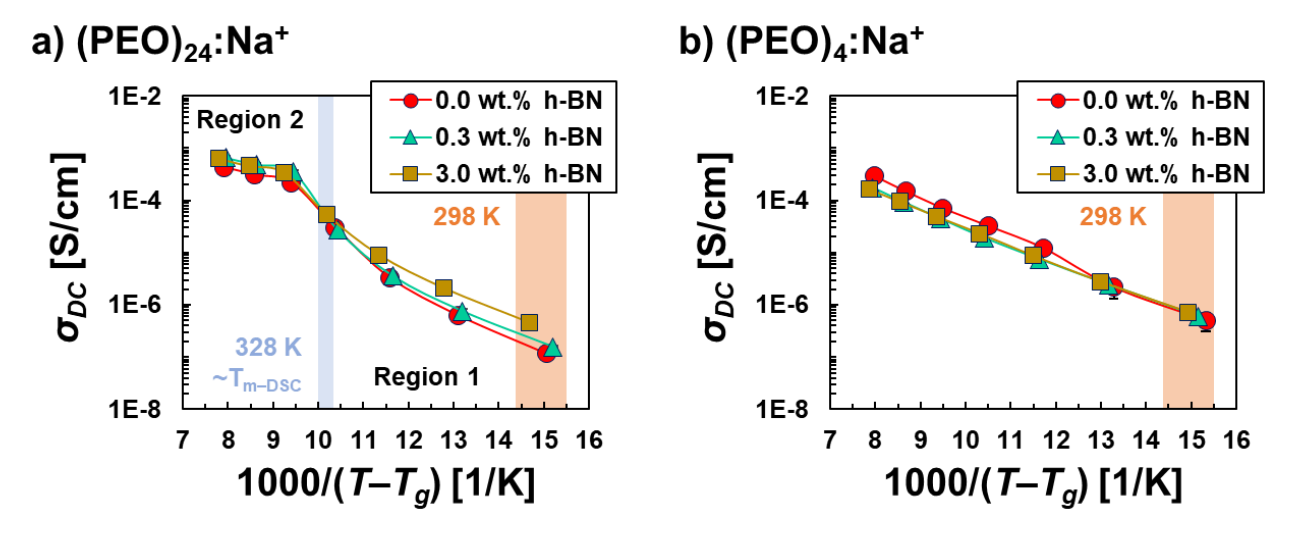


**Figure 5**. Arrhenius plots of total ionic conductivity  $\sigma$  for a) P(EO)<sub>24</sub>:Na<sup>+</sup> and b) P(EO)<sub>4</sub>:Na<sup>+</sup>. Orange regions in a) and b) indicate the range of room temperature as also indicated with text. Blue bar in a) indicates the melt transition (T<sub>m-DSC</sub>) region of the semicrystalline SPEs at ~328 K. Region 1 and Region 2 in a) represent the semicrystalline region and the amorphous region, respectively. Values reported are an average of two separate trials. Error bars represent one standard deviation of these two trials.

First, we focus on the P(EO)<sub>24</sub>:Na<sup>+</sup> salt concentration wherein all SPEs (i.e., with and without h–BN) are semicrystalline at room temperature. Based on our structural characterization results, we define two regions: Region 1 from 298 K (orange band) to 328 K (blue band) where the SPEs are semicrystalline, and Region 2 above 328 K where all samples are in the melt phase. The melt transition region is indicated in Figure 5a) as  $T_{m-DSC}$ .  $\sigma$  for all SPEs increases as temperature increases, in accordance with the thermal–dependence of ion–hopping. In Region 1, we observe that  $\sigma$  follows the trend  $\sigma_{3.0 \text{ wt.% h-BN}} > \sigma_{0.3 \text{ wt.% h-BN}} \sim \sigma_{0.0 \text{ wt.% h-BN}}$ , i.e., the SPEs containing h–BN exhibit higher  $\sigma$  than the h–BN–free SPE. Further, this behavior appears to scale with h–BN content, i.e., the SPE containing the highest weight loading of h–BN (3.0 wt.%) exhibits the highest  $\sigma$ . The absolute increment in  $\sigma$  going from 0.0 wt.% h–BN to 3.0 wt.% h–BN is ca. 4x. We attribute this increase in  $\sigma$  primarily to the positive effect of h–BN on the percentage of free charge carriers as shown in Figure 3 and Figure 4, i.e., h–BN aids in the dissociation of NaFSI, thereby generating more free charge carriers which can contribute to  $\sigma$ . While the  $T_g$ -scaled data takes into account changes in polymer segmental relaxation, we also normalized our data in Region 1 to the volume fraction of amorphous polymer which constitutes the primary ion–

conducting phase within the semicrystalline SPEs.  $^{60-62}$  This data (not shown) also reflects the same trend seen in Figure 5a), which suggests that the primary driving force behind enhanced  $\sigma$  is indeed the ability of h–BN to aid in salt dissociation. This trend prevails leading up to the melt transition of the SPEs, but the differences in  $\sigma$  become smaller in magnitude. Beyond this transition point, i.e., in Region 2, we observe that the data points nearly collapse into a single curve. This indicates that the role of h–BN on ion transport in the melt phase is negligible. The semicrystalline–to–amorphous transition of PEO with increasing temperature leads to a sharp increase in  $\sigma$  which is in agreement with previous reports on PEO–based semicrystalline SPEs.  $^{63, 64}$  Overall, our  $\sigma$  values are similar to those reported previously for PEO/NaFSI mixtures.  $^{53}$ 

Next, we focus on the P(EO)<sub>4</sub>:Na<sup>+</sup> salt concentration wherein all SPEs (i.e., with and without h–BN) are fully amorphous at room temperature, shown in Figure 5b). For these SPEs, we observe that  $\sigma$  initially follows the trend  $\sigma_{3.0 \text{ wt.% h-BN}} \sim \sigma_{0.3 \text{ wt.% h-BN}} \sim \sigma_{0.0 \text{ wt.% h-BN}}$ . This finding correlates well with Region 2 data for the P(EO)<sub>24</sub>:Na<sup>+</sup> SPEs which are also fully amorphous in that temperature region and exhibit only marginal changes in  $\sigma$  in the presence of h–BN. Above ca. 318 K, we find that  $\sigma_{0.0 \text{ wt.% h-BN}} > \sigma_{0.3 \text{ wt.% h-BN}} \sim \sigma_{3.0 \text{ wt.% h-BN}}$  across the remaining temperatures, i.e., the h–BN–containing SPEs are less ionically conductive than their h–BN–free counterpart. This finding correlates well with the decreasing PEO coordination percentage seen from our Raman spectroscopy analysis.

Direct comparison of  $\sigma$  for the two salt concentrations reveals that at 298 K,  $\sigma_{P(EO)4:Na}^+$  /  $\sigma_{P(EO)24:Na}^+$  = 3.25, i.e., the P(EO)4:Na<sup>+</sup> SPEs are on average 3.25x more ionically conductive than their P(EO)<sub>24</sub>:Na<sup>+</sup> counterparts. Although the exact percentage of free charge carriers is unclear for the P(EO)<sub>4</sub>:Na<sup>+</sup> SPEs, the semicrystalline nature of the P(EO)<sub>24</sub>:Na<sup>+</sup> SPEs is expected to influence this ratio. At 358 K where all SPEs at both salt concentrations are amorphous, this ratio flips to ca. 0.40, suggesting that in the melt, the SPEs with a lower salt concentration are more ionically conductive than SPEs containing a higher salt concentration.

Activation energies  $E_a$  for ion hopping obtained from experimental EIS data are shown in **Table 4** (see **Figure S7** and **Figure S8** in Supporting Information). We used Arrhenius fits for the  $P(EO)_{24}:Na^+$  SPEs and both Arrhenius and Vogel–Fulcher–Tammann (VFT) fits for the  $P(EO)_{4}:Na^+$  SPEs.<sup>27</sup>  $E_a$  for the  $P(EO)_{24}:Na^+$  SPEs has been calculated separately for Region 1 and Region 2 shown in Figure 5, whereas the entire temperature range is treated as having a single  $E_a$ 

for the P(EO)<sub>4</sub>:Na<sup>+</sup> SPEs. In Region 2,  $E_a$  is in the range of 0.31 eV and 0.36 eV, and decreases as the h–BN concentration increases. This trend suggests enhanced ion mobility as also supported by trends observed in our  $T_g$ –DSC results which indicates acceleration of polymer segmental mobility. These values agree well with those reported by Moreno et al for  $T > T_m$ .<sup>63</sup> In the semicrystalline state, i.e., Region 1, P(EO)<sub>24</sub>:Na<sup>+</sup> SPEs, the  $E_a$  increases by a factor of 4.5 (average) relative to Region 2, which we attribute to hindered ion transport due to PEO crystallites. Yet, the SPE containing the highest concentration of h–BN shows the lowest  $E_a$  indicating the positive effect of h–BN on overall ionic motion in the SPEs.

Table 4. Table of activation energies  $E_a$  for the SPEs. Arrhenius fits were used for the P(EO)<sub>24</sub>:Na<sup>+</sup> SPEs split into two regions. VFT fits were used for the P(EO)<sub>4</sub>:Na<sup>+</sup> SPEs.

a: Arrhenius Region 1; b: Arrhenius Region 2; c: Arrhenius; d: VFT; N/A: not applicable.

SPE	$E_a$ [eV]	$R^2$	$E_a$ [eV]	$R^2$	Tθ
	Region 1	Region 1	Region 2	Region 2	[K]
P(EO) <sub>24</sub> :Na <sup>+</sup> -0.0 wt.% h-BN	1.63 <sup>a</sup>	0.99	$0.36^{a}$	0.99	N/A
P(EO) <sub>24</sub> :Na <sup>+</sup> -0.3 wt.% h-BN	1.64 <sup>a</sup>	0.97	$0.33^{a}$	0.99	N/A
P(EO) <sub>24</sub> :Na <sup>+</sup> -3.0 wt.% h-BN	1.42 <sup>a</sup>	0.99	$0.31^{a}$	0.99	N/A
P(EO) <sub>4</sub> :Na <sup>+</sup> –0.0 wt.% h–BN	$1.61^{b}$	0.99	N/A	N/A	228
P(EO) <sub>4</sub> :Na <sup>+</sup> –0.3 wt.% h–BN	$3.56^{b}$	0.99	N/A	N/A	195
P(EO) <sub>4</sub> :Na <sup>+</sup> –3.0 wt.% h–BN	$1.95^{b}$	0.99	N/A	N/A	216

a: Arrhenius fit; b: VFT fit; N/A: not applicable.

For the P(EO)<sub>4</sub>:Na<sup>+</sup> SPEs, VFT fits yield  $E_a$  values as follows: 3.56 eV (0.3 wt.% h–BN) > 1.95 eV (3.0 wt.% h–BN) > 1.61 eV (0.0 wt.% h–BN), suggesting that the barrier to ion hopping is higher in the presence of h–BN than in its absence within the polymer matrix. Further, these  $E_a$  values are higher than those observed for the P(EO)<sub>24</sub>:Na<sup>+</sup> SPEs in the melt (Region 2), which we also observed using Arrhenius fits to the same data (see Figure S8 in Supporting Information). The exact reason behind these trends is unclear, but the local solvate structure and polymer backbone conformational changes could be contributing factors. Additionally, differences in polymer melt viscosity may also play an important role. These aspects will be reported in a separate study. The corresponding Vogel temperatures  $T_0$  for the P(EO)<sub>4</sub>:Na<sup>+</sup> SPEs are also shown for reference and are lower than the  $T_g$ –DSC values.

## 3.5 Transport Parameter Analysis

Composite SPEs are complex systems wherein multiple effects simultaneously influence  $\sigma$  in different ways. It is particularly important to understand whether improvements in  $\sigma$  are due to changes in ion mobility or changes in free charge carrier concentration, or both. This necessitates further analysis of the governing transport parameters, i.e., ion diffusion coefficient  $D_{ion}$  which represents ion mobility via the Einstein–Smoluchowski relation, and  $n_{free}$  which represents the number of free charge carriers in the SPEs. We use the MacDonald–Trukhan approach<sup>65, 66</sup> to quantify the transport parameters in our SPEs. This approach is based on analysis of the electrode polarization phenomenon in broadband dielectric (i.e., EIS) spectra, which relates  $D_{ion}$  to the maximum of the loss tangent via the equation:

$$D_{ion} = \frac{2\pi L^2 f_{max}}{32(\tan \delta)_{max}^3}$$

$$\boldsymbol{n_{free}} = \frac{\sigma k_B T}{D_{ion} e^2}$$

where L is the thickness of the SPE,  $f_{max}$  is the frequency corresponding to the maximum of the loss tangent,  $(tan \ \delta)_{max}$ , from dielectric spectra (see **Figure S9** in Supporting Information), e is electric charge,  $k_B$  is Boltzmann's constant, and T is temperature.  $D_{ion}$  can be combined with  $\sigma$  which is a measured quantity to estimate the free charge carrier concentration  $n_{free}$  in the SPEs. This approach has been used previously for similar analyses in electrolytes.  $^{67-73}$  These results are shown in **Figure 6**. We carried out the transport parameter analysis for two temperatures – 298 K

(25°C) and 328 K (55°C) – enabled by the collection of temperature–dependent EIS data shown in Figure 5. The loss tangent data beyond 328 K was saturated and thus could not be used for this analysis. Our structural characterization results reveal that at 298 K (25°C), the P(EO)<sub>24</sub>:Na<sup>+</sup> SPEs are semicrystalline whereas the P(EO)<sub>4</sub>:Na<sup>+</sup> SPEs are fully amorphous. However, the P(EO)<sub>24</sub>:Na<sup>+</sup> SPEs undergo melt transitions around 328 K (55°C) as seen from our DSC results (Figure 2). Thus, at this temperature we expect the P(EO)<sub>24</sub>:Na<sup>+</sup> SPEs to be amorphous and hence we focus our attention on this temperature first.

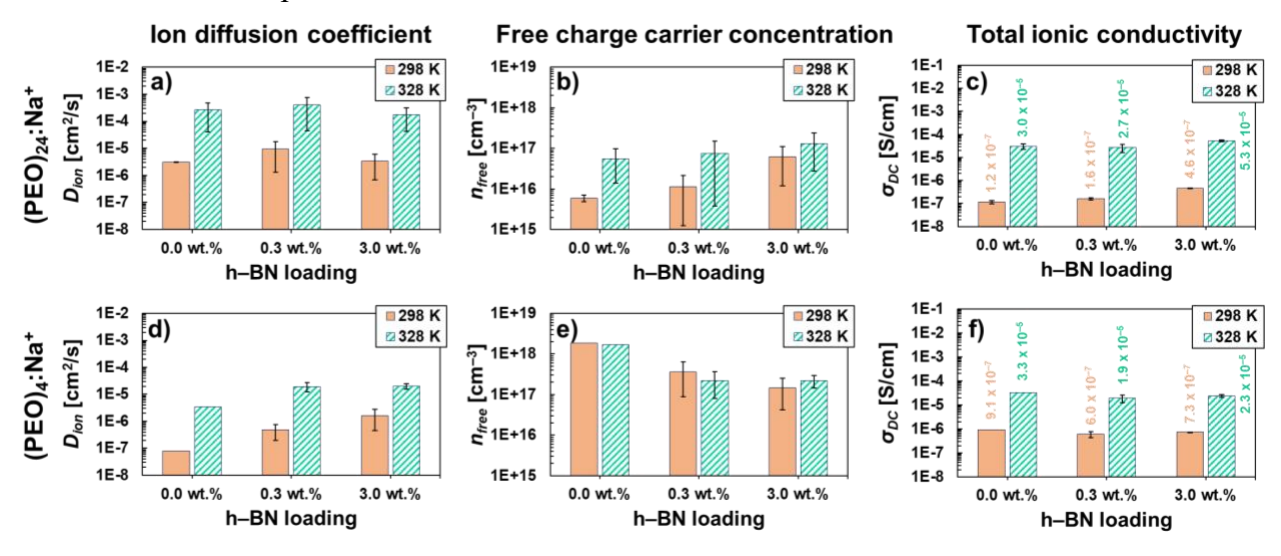


**Figure 6.** Summary of ion transport parameters for the two salt concentrations investigated: top row shows  $P(EO)_{24}$ : Na<sup>+</sup> and bottom row shows  $P(EO)_{4}$ :Na<sup>+</sup>. Columns (L–R) represent ion diffusion coefficient  $D_{ion}$ , free charge carrier concentration  $n_{free}$ , and total ionic conductivity  $\sigma_{DC}$  (referred to as  $\sigma$  in the text). Values reported are an average of two separate trials except for  $P(EO)_{4}$ :Na<sup>+</sup>–0.0 wt.% h–BN at 298 K and 328 K which are from a single trial. Error bars represent one standard deviation of the two trials.

It is important to first discuss the factors that affect  $D_{ion}$ . In an amorphous polymer matrix containing dispersed filler,  $D_{ion}$  is correlated with polymer segmental dynamics, melt viscosity, and the tortuosity generated by filler particles. Suppression of polymer  $T_g$  and melt viscosity enhance  $D_{ion}$ , whereas tortuosity suppresses  $D_{ion}$ . An additional factor for semicrystalline polymers is polymer crystallinity, which also suppresses  $D_{ion}$ . Therefore, we discuss our results in the context of these parameters. Figure 6, top row shows data for the  $P(EO)_{24}$ :Na<sup>+</sup> SPEs. At 328 K (55°C) (green bars), we observe that  $D_{ion}$  is in the range of  $10^{-4}$  cm<sup>2</sup>/s for SPEs with and without h–BN (Figure 6a)). Within error,  $D_{ion}$  appears to remain invariant with the addition of 0.3 wt.% h–BN flakes suggesting that the effect of h–BN on ion diffusivity at 328 K is negligible. At 3.0 wt.% h–BN, there appears to be a small decrease (0.6x) in  $D_{ion}$  relative to the 0.3 wt.% h–BN SPE which

may either be due to the tortuosity generated by the flakes, and/or a higher melt viscosity due to more h-BN flakes. The changes in  $T_g$  here are small and therefore their effect on ion mobility is also likely small. Going from 328 K (amorphous) to 298 K (semicrystalline), Dion decreases by two orders of magnitude to ca.  $10^{-6}$  cm<sup>2</sup>/s, which is in accordance with the temperature–dependent **D**ion values reported for Na SPEs. 74-76 At 0.3 wt.% h-BN, **D**ion increases by 3x although polymer crystallinity also increases. A plausible explanation for this increase is changes to PEO conformations induced by h-BN as we have reported previously.<sup>22</sup> At 3.0 wt.% h-BN, **D**ion decreases by 0.65x relative to the 0.3 wt.% h–BN sample which may be due to tortuosity generated by the h-BN flakes. These changes are small, and also complicated by polymer crystallinity which makes their isolation a challenge. Yet, this value is similar to that of the h-BN-free SPE which indicates that at 298 K, 3.0 wt.% h-BN does not significantly influence ion mobility. This trend is similar to that seen at 328 K. Next, we analyze  $n_{free}$ , which lies in the range of  $10^{16}$  cm<sup>-3</sup>– $10^{17}$  cm<sup>-</sup> <sup>3</sup>. n<sub>free</sub> at 328 K is invariant for the 0.0 wt.% h–BN and 0.3 wt.% h–BN SPEs. However, the highest nfree value is observed for the 3.0 wt.% h-BN SPE, which is about 2.3x higher relative to the h-BN-free SPE. The combined effect of these transport parameters is seen in Figure 6c), wherein  $\sigma$ at 328 K for the 0.0 wt.% h-BN SPE and the 0.3 wt.% h-BN SPE are similar, but there is an increase in  $\sigma$  at 3.0 wt.% h–BN by ca. 1.76x relative to the other two SPEs.

For the P(EO)<sub>24</sub>:Na<sup>+</sup> SPEs at 298 K (25°C) (solid orange bars), observe that  $n_{free}$  remains invariant with the addition of 0.3 wt.% h–BN but increases by 6x for the 3.0 wt.% h–BN SPE. This increased  $n_{free}$  translates to a concomitant 4x increase in  $\sigma$  at 298 K as seen in Figure 6c). The h–BN–free SPE and the 3.0 wt.% h–BN SPE are equivalent in terms of polymer crystallinity (ca. 30%). Further, since  $D_{ion}$  for the h–BN–free and 3.0 wt.% h–BN SPE are similar, this increase in  $\sigma$  is primarily driven by the increase in  $n_{free}$  thereby reinforcing the h–BN–'assisted' salt dissociation mechanism we proposed in Section 3.3.

Next, we focus on the P(EO)<sub>4</sub>:Na<sup>+</sup> SPEs shown in Figure 6, bottom row. All SPEs are amorphous at this salt concentration (across all temperatures) and we expect no effects from polymer crystallinity. At 328 K (55°C) (green bars), the *D<sub>ion</sub>* for these SPEs both with and without h–BN lies in the range of 10<sup>-6</sup> cm<sup>2</sup>/s–10<sup>-5</sup> cm<sup>2</sup>/s (Figure 6d)). At 298 K (25°C) (orange bars), *D<sub>ion</sub>* decreases to ca. 10<sup>-7</sup> S/cm–10<sup>-6</sup> S/cm relative to 328 K, a decrease also seen for the P(EO)<sub>24</sub>:Na<sup>+</sup> SPEs. These values are lower than those of the P(EO)<sub>24</sub>:Na<sup>+</sup> SPEs at the same temperature which

is likely due to differences in viscosity based on salt concentration. This difference may also help explain the higher  $E_a$  values reported in Table 4 for this salt concentration. We observe that  $D_{ion}$  increases by ca. 6x with increase in h–BN loading at both temperatures. This increase is not seen for the amorphous  $P(EO)_{24}:Na^+$  SPEs which turns our attention to the significantly different solvation environments in these two sets of SPEs. In the SSIP–dominated SPEs, ion motion occurs primarily via polymer segmental motion as in the case of dilute electrolytes. On the other hand, theoretical analysis<sup>77</sup> suggests that ion transport in highly concentrated sodium electrolytes occurs via a ligand–exchange mechanism facilitated by AGGs wherein the diffusive dynamics of ions are different than in dilute electrolytes. This may be one reason for the increasing  $D_{ion}$  trend seen at this salt concentration although the ionic conductivity  $\sigma$  appears to remain invariant. Next, we focus on  $n_{free}$ . In Figure 6e), we observe that  $n_{free}$  lies in the range of  $10^{17}$  cm<sup>-3</sup>– $10^{18}$  cm<sup>-3</sup> which is higher than the corresponding  $P(EO)_{24}:Na^+$  SPEs, and decreases at 328 K with the addition of h–BN. As seen in Figure 6f),  $\sigma$  at 328 K decreases, albeit marginally, with the addition of h–BN flakes to the SPEs. Therefore, these results suggest that effects from thermal energy overpower any effects from the h–BN flakes at 328 K.

To contextualize these findings, recent computational work<sup>78</sup> on PEO–LiTFSI– nanoparticle melts suggests that silica nanoparticles (Lewis acidic) cause a decrease in  $\sigma$  owing to nanoparticle—ion association, with which our results appear to align given the partial Lewis acidity of h–BN.  $n_{free}$  at 298 K appears to decrease with an increase in h–BN loading, with the largest decrease being observed going from 0.0 wt.% h–BN to 0.3 wt.% h–BN. This trend agrees with the increasing CIPs fraction determined from our Raman spectroscopy results with the assumption that the CIPs increase at the cost of any free ions (SSIPs).

It is important to note that the MacDonald–Trukhan approach was originally designed for dilute electrolytes and does not account for ion–ion correlations. Sokolov and coworkers<sup>70, 71</sup> have incorporated an empirical correction factor into this equation to better represent highly–concentrated electrolytes that are typical in battery applications. Yet, they report that the MacDonald–Trukhan approach can only be used as a qualitative means of analysis especially at high salt concentrations (>5 wt.% salt). Thus, we reason that our transport parameter analysis is also constrained by the limitations of the MacDonald–Trukhan approach, which for instance reflects in the higher *Dion* values observed here relative to NMR–derived values. Further work on

obtaining more representative data using NMR techniques is in progress. Yet, this analysis provides important insight about decoupling the effects of  $D_{ion}$  and  $n_{free}$  on  $\sigma$ . Lastly, Figure 6f) shows that within error,  $\sigma$  at 298 K does not change with the addition of h–BN likely due to an increase in the CIP fraction and a decrease in  $n_{free}$  although  $D_{ion}$  increases. The significant finding here is that the  $n_{free}$  contribution dominates  $\sigma$  more so for the P(EO)<sub>24</sub>:Na<sup>+</sup> SPEs. Of note is the finding that the largest improvement in  $\sigma$  is obtained when  $n_{free}$  is maximized (as opposed to the case wherein  $D_{ion}$  is maximized), which directly relates to the importance of filler chemistry, in this case, the dual–Lewis h–BN.

The temperature–dependence of  $\sigma$  for the two salt concentrations is also discussed here.  $\sigma$  for the P(EO)<sub>24</sub>:Na<sup>+</sup> SPEs increases by 2 orders of magnitude going from 298 K (10<sup>-7</sup> S/cm) to 328 K (10<sup>-5</sup> S/cm), whereas for the P(EO)<sub>4</sub>:Na<sup>+</sup> SPEs this increase is only 1 order of magnitude (ca.  $10^{-6}$  S/cm) to ( $10^{-5}$  S/cm). We posit that the larger increase at lower salt concentration is due to the semicrystalline–to–amorphous phase–transition as well as a lower melt viscosity. The  $E_a$  values for P(EO)<sub>24</sub>:Na<sup>+</sup> SPEs in Region 2 being lower than the P(EO)<sub>24</sub>:Na<sup>+</sup> SPEs (see Table 4) further supports this argument.

In this section, we investigated the total ionic conductivity of our SPEs and carried out rigorous analysis of the underlying transport parameters using the MacDonald–Trukhan approach. At 298 K,  $n_{free}$  increases,  $D_{ion}$  remains invariant, and  $\sigma$  increases as h–BN loading increases for the P(EO)<sub>24</sub>:Na<sup>+</sup> SPEs. A similar effect is observed at 328 K, but to a smaller extent. Therefore, this increase in  $\sigma$  is most likely from an increase in  $n_{free}$ . On the other hand for the P(EO)<sub>4</sub>:Na<sup>+</sup> SPEs at 298 K,  $n_{free}$  decreases,  $D_{ion}$  increases, and  $\sigma$  remains invariant as h–BN loading increases suggesting that maximizing  $n_{free}$  is necessary to maximize  $\sigma$ .

#### 4. Conclusions

In this fundamental study, we carried out a thorough structural and electrochemical characterization of PEO/NaFSI/h–BN SPEs at EO:Na<sup>+</sup> concentrations of 24:1 and 4:1. In the h–BN concentration range that we investigate (below than the percolation threshold), our XRD and DSC results reveal that PEO crystallinity in semicrystalline PEO/h–BN polymer (electrolyte) composites follows a non–monotonic trend with respect to h–BN concentration. We attribute this trend to competing effects between heterogeneous nucleation at low h–BN loading and spherulitic

confinement at high h–BN loading, caused by the h–BN flakes. A key observation is that h–BN does not induce crystallinity at the EO:Na<sup>+</sup> concentration of 4:1 which we posit is due to the dominant effect of polymer–cation complexation.

We also investigated the solvation structure in our SPEs using Raman spectroscopy. The P(EO)<sub>24</sub>:Na<sup>+</sup> SPEs comprise solvent–separated ion pairs and contact ion pairs, whereas the PEO<sub>4</sub>:Na<sup>+</sup> SPEs comprise CIPs and AGGs. We find that the addition of h–BN flakes improves salt dissociation in the PEO<sub>24</sub>:Na<sup>+</sup> SPEs in addition to influencing PEO crystallinity. On the other hand, it appears that h–BN leads to an increase in CIP fractions in the fully amorphous PEO<sub>4</sub>:Na<sup>+</sup> SPEs which calls into question the timescales associated with ion dissociation and ion recombination in composite SPEs. We also obtained molecular–level insight into the effect of h–BN on speciation using DFT calculations which reveal that h–BN binds favorably with dissociated cations, dissociated anions, as well as PEO. Based on these findings, we propose that the underlying mechanism behind the experimentally–observed increase in free charge carrier concentrations is an h–BN–'assisted' salt dissociation process wherein PEO and h–BN work synergistically to dissociate NaFSI whose dissociation energy is similar in the presence of h–BN.

Lastly, we have found that the total ionic conductivity of our SPEs increases by ca. 2x-4x in the presence of h–BN relative to h–BN–free SPEs depending upon the temperature, despite possible tortuosity from the filler particles. Detailed transport parameter analysis based on the MacDonald–Trukhan approach provides additional insight into the underlying ion dynamics and  $\sigma$  results. To contextualize these findings, we note that the largest improvement in total ionic conductivity is observed at the EO:Na<sup>+</sup> ratio of 24:1 where the SPEs are semicrystalline and therefore mechanically robust relative to the 4:1 SPEs. The PEO<sub>4</sub>:Na<sup>+</sup> SPEs do not show improvement in total ionic conductivity likely because the PEO chains are at saturation for complexation.

Using a combination of experiment and computation, this work provides key insight into how Lewis–active fillers like h–BN can affect ionic conductivity in dual–ion conducting polymer electrolytes. This work shows that the SPEs transition from solvent–separated ion pair– to contact ion pair–dominated regimes with increasing salt concentration. If ionic aggregates can be engineered to percolate using h–BN, the resulting ion channels can allow for rapid transport and thus higher ion conductivity. <sup>79,80</sup> Further, h–BN has shown promise as an additive to SPEs because

it can regulate cation transport in alkali batteries. Because h–BN binds both ion species, the evolution of the solid electrolyte interface (SEI) upon charge/discharge should be investigated. Future work on both topics is currently underway. In conclusion, this study reveals complex structure–property relationships in SPEs containing Lewis–active filler. A small concentration of dual–Lewis h–BN yields a total ionic conductivity of 0.35 mS/cm at 65°C in our model SPE, highlighting the impact of filler chemistry on ion transport properties in such systems.

#### Acknowledgements

The authors are grateful to the National Science Foundation (NSF) under Future Manufacturing grant NSF–FMRG–2134715 (SP, RJC) with PI Prof. E. Detsi, the Division of Materials Research Polymers Program under grants NSF–DMR–1905912 (RJC) and NSF–DMR–2407300 (RJC), and the Vagelos Integrated Program in Energy Research (VIPER) undergraduate research program at the University of Pennsylvania (CS) for supporting this work. The authors acknowledge use of the Dual Source and Environmental X–ray Scattering facility operated by the Laboratory for Research on the Structure of Matter at the University of Pennsylvania (NSF–MRSEC–DMR–2309043). Additionally, this work made use of resources at the Singh Center for Nanotechnology at the University of Pennsylvania, which is supported by the NSF National Nanotechnology Coordinated Infrastructure Program under grant NSF–NNCI–2025608. All computational work in this paper was carried out on the FASRC Cannon cluster supported by the FAS Division of Science Research Computing Group at Harvard University, USA (GP).

# **Supporting Information**

Differential DSC curves; Raw Raman spectra; Deconvoluted Raman spectra for the PEO region; Tricomponent DFT calculations; Raw Bode plots from EIS for selected temperatures; Arrhenius and VFT fits to EIS data; Representative loss tangent plots from EIS.

#### References

- 1. Yabuuchi, N., Kubota, K., Dahbi, M. and Komaba, S., 2014. Research Development on Sodium-ion Batteries. *Chemical Reviews*, 114(23), pp.11636-11682. <a href="https://doi.org/10.1021/cr500192f">https://doi.org/10.1021/cr500192f</a>.
- **2.** Vaalma, C., Buchholz, D., Weil, M. and Passerini, S., **2018**. A Cost and Resource Analysis of Sodium-ion Batteries. *Nature Reviews Materials*, *3*(4), pp.1-11. https://doi.org/10.1038/natrevmats.2018.13.
- **3.** Tarascon, J.M., **2020**. Na-ion versus Li-ion Batteries: Complementarity Rather than Competitiveness. *Joule*, 4(8), pp.1616-1620. <a href="https://doi.org/10.1016/j.joule.2020.06.003">https://doi.org/10.1016/j.joule.2020.06.003</a>.
- **4.** Qin, H. and Panzer, M.J., **2020**. Zwitterionic Copolymer-Supported Ionogel Electrolytes Featuring a Sodium Salt/Ionic Liquid Solution. *Chemistry of Materials*, *32*(18), pp.7951-7957. https://doi.org/10.1021/acs.chemmater.0c02820.
- Zhao, Y., Kang, Y., Wozny, J., Lu, J., Du, H., Li, C., Li, T., Kang, F., Tavajohi, N. and Li, B.,
   2023. Recycling of Sodium-ion Batteries. *Nature Reviews Materials*, 8(9), pp.623-634. https://doi.org/10.1038/s41578-023-00574-w.
- **6.** Yang, C., Xin, S., Mai, L. and You, Y., **2021**. Materials Design for High-Safety Sodium-Ion Battery. *Advanced Energy Materials*, *11*(2), p.2000974. https://doi.org/10.1002/aenm.202000974.
- 7. Armand, M., 1983. Polymer Solid Electrolytes-An Overview. *Solid State Ionics*, 9, pp.745-754. <a href="https://doi.org/10.1016/0167-2738(83)90083-8">https://doi.org/10.1016/0167-2738(83)90083-8</a>.
- **8.** Ratner, M.A. and Shriver, D.F., **1988**. Ion transport in Solvent-Free Polymers. *Chemical Reviews*, 88(1), pp.109-124. <a href="https://doi.org/10.1021/cr00083a006">https://doi.org/10.1021/cr00083a006</a>.
- **9.** Hallinan Jr, D.T. and Balsara, N.P., **2013**. Polymer Electrolytes. *Annual Review of Materials Research*, *43*, pp.503-525. <a href="https://doi.org/10.1146/annurev-matsci-071312-121705">https://doi.org/10.1146/annurev-matsci-071312-121705</a>.
- **10.** Bresser, D., Lyonnard, S., Iojoiu, C., Picard, L. and Passerini, S., **2019**. Decoupling Segmental Relaxation and Ionic Conductivity for Lithium-Ion Polymer Electrolytes. *Molecular Systems Design & Engineering*, *4*(4), pp.779-792. <a href="https://doi.org/10.1039/C9ME00038K">https://doi.org/10.1039/C9ME00038K</a>.
- **11.** Bocharova, V. and Sokolov, A.P., **2020**. Perspectives for Polymer Electrolytes: A View from Fundamentals of Ionic Conductivity. *Macromolecules*, *53*(11), pp.4141-4157. https://doi.org/10.1021/acs.macromol.9b02742.
- **12.** France-Lanord, A., Wang, Y., Xie, T., Johnson, J.A., Shao-Horn, Y. and Grossman, J.C., **2019**. Effect of Chemical Variations in the Structure of Poly (Ethylene Oxide)-Based Polymers on Lithium Transport in Concentrated Electrolytes. *Chemistry of Materials*, *32*(1), pp.121-126. <a href="https://doi.org/10.1021/acs.chemmater.9b02645">https://doi.org/10.1021/acs.chemmater.9b02645</a>.
- **13.** Chen, H., Jiang, D.E., Yang, Z. and Dai, S., **2022**. Engineering Nanostructured Interfaces of Hexagonal Boron Nitride-Based Materials for Enhanced Catalysis. *Accounts of Chemical Research*, *56*(1), pp.52-65. <a href="https://doi.org/10.1021/acs.accounts.2c00564">https://doi.org/10.1021/acs.accounts.2c00564</a>.
- **14.** Golberg, D., Bando, Y., Huang, Y., Terao, T., Mitome, M., Tang, C. and Zhi, C., **2010**. Boron Nitride Nanotubes and Nanosheets. *ACS Nano*, *4*(6), pp.2979-2993. <a href="https://doi.org/10.1021/nn1006495">https://doi.org/10.1021/nn1006495</a>.
- **15.** Vijayakumar, V., Ghosh, M., Asokan, K., Sukumaran, S.B., Kurungot, S., Mindemark, J., Brandell, D., Winter, M. and Nair, J.R., **2023**. 2D Layered Nanomaterials as Fillers in Polymer Composite Electrolytes for Lithium Batteries. *Advanced Energy Materials*, *13*(15), p.2203326. https://doi.org/10.1002/aenm.202203326.
- 16. Ma, L., Tan, J., Wang, Y., Liu, Z., Yang, Y., Gray, T., Zhang, X., Ye, M. and Shen, J., 2023. Boron-Based High-Performance Lithium Batteries: Recent Progress, Challenges, and

- Perspectives. *Advanced Energy Materials*, *13*(25), p.2300042. https://doi.org/10.1002/aenm.202300042.
- **17.** Chen, S., Feng, F., Yin, Y., Lizo, X. and Ma, Z., **2019**. Plastic Crystal Polymer Electrolytes Containing Boron Based Anion Acceptors for Room Temperature All-Solid-State Sodium-Ion Batteries. *Energy*Storage

  Materials, 22, pp.57-65. https://doi.org/10.1016/j.ensm.2018.12.023.
- **18.** Chen, S., Feng, F., Che, H., Yin, Y. and Ma, Z.F., **2021**. High Performance Solid-State Sodium Batteries Enabled by Boron Contained 3D Composite Polymer Electrolyte. *Chemical Engineering Journal*, *406*, p.126736. <a href="https://doi.org/10.1016/j.cej.2020.126736">https://doi.org/10.1016/j.cej.2020.126736</a>.
- **19.** Genier, F.S., Pathreeker, S., Adebo, P.O., Chando, P. and Hosein, I.D., **2022**. Design of a Boron-Containing PTHF-Based Solid Polymer Electrolyte for Sodium-Ion Conduction with High Na<sup>+</sup> Mobility and Salt Dissociation. *ACS Applied Polymer Materials*, *4*(10), pp.7645-7663. <a href="https://doi.org/10.1021/acsapm.2c01276">https://doi.org/10.1021/acsapm.2c01276</a>.
- **20.** Yang, M., Feng, F., Ren, Y., Chen, S., Chen, F., Chu, D., Guo, J., Shi, Z., Cai, T., Zhang, W. and Ma, Z.F., Chen, S., and Liu., T. **2023**. Coupling Anion-Capturer with Polymer Chains in Fireproof Gel Polymer Electrolyte Enables Dendrite-Free Sodium Metal Batteries. *Advanced Functional Materials*, *33*(46), p.2305383. <a href="https://doi.org/10.1002/adfm.202305383">https://doi.org/10.1002/adfm.202305383</a>.
- **21.** Guo, J., Feng, F., Jiang, X., Wang, R., Chu, D., Ren, Y., Chen, F., He, P., Ma, Z.F., Chen, S. and Liu, T., **2024**. Boosting Selective Na<sup>+</sup> Migration Kinetics in Structuring Composite Polymer Electrolyte Realizes Ultrastable All-Solid-State Sodium Batteries. *Advanced Functional Materials*, p.2313496. <a href="https://doi.org/10.1002/adfm.202313496">https://doi.org/10.1002/adfm.202313496</a>.
- **22.** Pathreeker, S., Snyder, C.A., Papamokos, G.V. and Composto, R.J., **2023**. Hexagonal Boron Nitride Modulates Crystallinity and Charge Mobility in Poly (ethylene oxide)–NaNO<sub>3</sub> Electrolytes. *The Journal of Physical Chemistry C*, *128*(1), pp.38-49. https://doi.org/10.1021/acs.jpcc.3c06455.
- 23. Shriver, D.F., Papke, B.L., Ratner, M.A., Dupon, R., Wong, T. and Brodwin, M., 1981. Structure and Ion Transport in Polymer-Salt complexes. *Solid State Ionics*, 5, pp.83-88. <a href="https://doi.org/10.1016/0167-2738(81)90199-5">https://doi.org/10.1016/0167-2738(81)90199-5</a>.
- **24.** Martinez-Ibañez, M., Boaretto, N., Meabe, L., Wang, X., Zhu, H., Santiago, A., Zugazua, O., Forsyth, M., Armand, M. and Zhang, H., **2022**. Revealing the Anion Chemistry Effect on Transport Properties of Ternary Gel Polymer Electrolytes. *Chemistry of Materials*, *34*(16), pp.7493-7502. https://doi.org/10.1021/acs.chemmater.2c00260.
- **25.** Mendes, R.A., Dias, L.G., Da Silva, J.L. and Siqueira, L.J., **2023**. Sodium-Ion Electrolytes based on Poly-Ethylene Oxide Oligomers in Dual-Carbon Cells: Anion Size Drives the Charging Behavior. *Nano Energy*, *118*, p.108957. https://doi.org/10.1016/j.nanoen.2023.108957.
- **26.** Kmiec, S., Ruoff, E., Darga, J., Bodratti, A. and Manthiram, A., **2023**. Scalable Glass-Fiber-Polymer Composite Solid Electrolytes for Solid-State Sodium–Metal Batteries. *ACS Applied Materials & Interfaces*, *15*(17), pp.20946-20957. <a href="https://doi.org/10.1021/acsami.3c00240">https://doi.org/10.1021/acsami.3c00240</a>.
- **27.** Yang, M. and Epps III, T.H., **2024**. Solid-State, Single-Ion Conducting, Polymer Blend Electrolytes with Enhanced Li<sup>+</sup> Conduction, Electrochemical Stability, and Limiting Current Density. *Chemistry of Materials*. https://doi.org/10.1021/acs.chemmater.3c02389.
- **28.** Wright, P.V., **1975**. Electrical Conductivity in Ionic Complexes of Poly (ethylene oxide). *British Polymer Journal*, 7(5), pp.319-327. https://doi.org/10.1002/pi.4980070505.
- **29.** Gadjourova, Z., Martín y Marero, D., Andersen, K.H., Andreev, Y.G. and Bruce, P.G., **2001**. Structures of the Polymer Electrolyte Complexes PEO<sub>6</sub>: LiXF<sub>6</sub> (X= P, Sb), Determined from

- Neutron Powder Diffraction Data. *Chemistry of Materials*, 13(4), pp.1282-1285. https://doi.org/10.1021/cm000949k.
- **30.** Halat, D.M., Snyder, R.L., Sundararaman, S., Choo, Y., Gao, K.W., Hoffman, Z.J., Abel, B.A., Grundy, L.S., Galluzzo, M.D., Gordon, M.P. and Celik, H., **2021**. Modifying Li<sup>+</sup> and Anion Diffusivities in Polyacetal Electrolytes: A Pulsed-Field-Gradient NMR Study of Ion Self-Diffusion. *Chemistry* of *Materials*, *33*(13), pp.4915-4926. https://doi.org/10.1021/acs.chemmater.1c00339.
- **31.** Jang, S., Hernandez Alvarez, E.I., Chen, C., Jing, B.B., Shen, C., Braun, P.V., Schleife, A., Schroeder, C.M. and Evans, C.M., **2023**. Control of Lithium Salt Partitioning, Coordination, and Solvation in Vitrimer Electrolytes. *Chemistry of Materials*, *35*(19), pp.8039-8049. <a href="https://doi.org/10.1021/acs.chemmater.3c01353">https://doi.org/10.1021/acs.chemmater.3c01353</a>.
- **32.** Wu, Y., Wagner, L.K. and Aluru, N.R., **2015**. The Interaction Between Hexagonal Boron Nitride and Water from First Principles. *The Journal of Chemical Physics*, *142*(23). https://doi.org/10.1063/1.4922491.
- **33.** Boys, S.F. and Bernardi, F.J.M.P., **1970**. The Calculation of Small Molecular Interactions by the Differences of Separate Total Energies. Some Procedures with Reduced Errors. *Molecular Physics*, *19*(4), pp.553-566. https://doi.org/10.1080/00268977000101561.
- **34.** Pipertzis, A., Papamokos, G., Mühlinghaus, M., Mezger, M., Scherf, U. and Floudas, G., **2020**. What Determines the Glass Temperature and DC-Conductivity in Imidazolium-Polymerized Ionic Liquids with a Polythiophene Backbone?. *Macromolecules*, *53*(9), pp.3535-3550. <a href="https://doi.org/10.1021/acs.macromol.0c00226">https://doi.org/10.1021/acs.macromol.0c00226</a>.
- **35.** Pipertzis, A., Papamokos, G., Sachnik, O., Allard, S., Scherf, U. and Floudas, G., **2021**. Ionic Conductivity in Polyfluorene-Based Diblock Copolymers Comprising Nanodomains of a Polymerized Ionic Liquid and a Solid Polymer Electrolyte Doped with LiTFSI. *Macromolecules*, *54*(9), pp.4257-4268. https://doi.org/10.1021/acs.macromol.1c00436.
- **36.** Jancar, J., Douglas, J.F., Starr, F.W., Kumar, S.K., Cassagnau, P., Lesser, A.J., Sternstein, S.S. and Buehler, M.J., **2010**. Current Issues in Research on Structure–property Relationships in Polymer Nanocomposites. *Polymer*, *51*(15), pp.3321-3343. https://doi.org/10.1016/j.polymer.2010.04.074.
- **37.** Gam, S., Meth, J.S., Zane, S.G., Chi, C., Wood, B.A., Seitz, M.E., Winey, K.I., Clarke, N. and Composto, R.J., **2011**. Macromolecular Diffusion in A Crowded Polymer Nanocomposite. *Macromolecules*, *44*(9), pp.3494-3501. <a href="https://doi.org/10.1021/ma102463q">https://doi.org/10.1021/ma102463q</a>.
- **38.** Kumar, S.K., Benicewicz, B.C., Vaia, R.A. and Winey, K.I., **2017**. 50<sup>th</sup> Anniversary Perspective: Are Polymer Nanocomposites Practical for Applications?. *Macromolecules*, 50(3), https://doi.org/10.1021/acs.macromol.6b02330.
- **39.** Tu, C.H., Steinhart, M., Berger, R., Kappl, M., Butt, H.J. and Floudas, G., **2023**. When Crystals Flow. *Science Advances*, *9*(19), p.eadg8865. <a href="https://doi.org/10.1126/sciadv.adg8865">https://doi.org/10.1126/sciadv.adg8865</a>.
- **40.** Choi, B.K., **2004**. Optical Microscopy Study on the Crystallization in PEO-Salt Polymer Electrolytes. *Solid* State Ionics, 168(1-2), pp.123-129. https://doi.org/10.1016/j.ssi.2004.01.026.
- **41.** Marzantowicz, M., Dygas, J.R., Krok, F., Nowiński, J.L., Tomaszewska, A., Florjańczyk, Z. and Zygadło-Monikowska, E., **2006**. Crystalline Phases, Morphology and Conductivity of PEO: LiTFSI Electrolytes in the Eutectic Region. *Journal of Power Sources*, *159*(1), pp.420-430. <a href="https://doi.org/10.1016/j.jpowsour.2006.02.044">https://doi.org/10.1016/j.jpowsour.2006.02.044</a>.

- **42.** Celzard, A., McRae, E., Deleuze, C., Dufort, M., Furdin, G. and Marêché, J.F., **1996**. Critical Concentration in Percolating Systems Containing a High-Aspect-Ratio Filler. *Physical Review B*, *53*(10), p.6209. <a href="https://doi.org/10.1103/PhysRevB.53.6209">https://doi.org/10.1103/PhysRevB.53.6209</a>.
- **43.** Cheng, S., Smith, D.M. and Li, C.Y., **2015**. Anisotropic Ion Transport in a Poly (Ethylene Oxide)—LiClO<sub>4</sub> Solid State Electrolyte Templated by Graphene Oxide. *Macromolecules*, 48(13), pp.4503-4510. https://doi.org/10.1021/acs.macromol.5b00972.
- **44.** Ning, N., Fu, S., Zhang, W., Chen, F., Wang, K., Deng, H., Zhang, Q. and Fu, Q., **2012**. Realizing the Enhancement of Interfacial Interaction in Semicrystalline Polymer/Filler Composites via Interfacial Crystallization. *Progress in Polymer Science*, *37*(10), pp.1425-1455. <a href="https://doi.org/10.1016/j.progpolymsci.2011.12.005">https://doi.org/10.1016/j.progpolymsci.2011.12.005</a>.
- **45.** Tong, Y., Lin, Y., Wang, S. and Song, M., **2015**. A study of Crystallisation of Poly (Ethylene Oxide) and Polypropylene on Graphene Surface. *Polymer*, *73*, pp.52-61. https://doi.org/10.1016/j.polymer.2015.07.025.
- **46.** Huang, Z., Wang, S., Kota, S., Pan, Q., Barsoum, M.W. and Li, C.Y., **2016**. Structure and Crystallization Behavior of Poly (Ethylene Oxide)/Ti<sub>3</sub>C<sub>2</sub>T<sub>x</sub> MXene Nanocomposites. *Polymer*, *102*, pp.119-126. https://doi.org/10.1016/j.polymer.2016.09.011.
- **47.** Pan, Q., Zheng, Y., Kota, S., Huang, W., Wang, S., Qi, H., Kim, S., Tu, Y., Barsoum, M.W. and Li, C.Y., **2019**. 2D MXene-Containing Polymer Electrolytes for All-Solid-State Lithium Metal Batteries. *Nanoscale Advances*, *1*(1), pp.395-402. https://doi.org/10.1039/C8NA00206A.
- **48.** Biccai, S., Boland, C.S., O'Driscoll, D.P., Harvey, A., Gabbett, C., O'Suilleabhain, D.R., Griffin, A.J., Li, Z., Young, R.J. and Coleman, J.N., **2019**. Negative Gauge Factor Piezoresistive Composites Based on Polymers Filled with MoS<sub>2</sub> Nanosheets. *ACS Nano*, *13*(6), pp.6845-6855. <a href="https://doi.org/10.1021/acsnano.9b01613">https://doi.org/10.1021/acsnano.9b01613</a>.
- **49.** Tian, Z., Zou, Y., Liu, G., Wang, Y., Yin, J., Ming, J. and Alshareef, H.N., **2022**. Electrolyte Solvation Structure Design for Sodium Ion Batteries. *Advanced Science*, *9*(22), p.2201207. <a href="https://doi.org/10.1002/advs.202201207">https://doi.org/10.1002/advs.202201207</a>.
- **50.** Koenig, J.L. and Angood, A.C., **1970**. Raman Spectra of Poly (Ethylene Glycols) in Solution. *Journal of Polymer Science Part A-2: Polymer Physics*, 8(10), pp.1787-1796. https://doi.org/10.1002/pol.1970.160081013.
- **51.** Han, S.D., Sommer, R.D., Boyle, P.D., Zhou, Z.B., Young, V.G., Borodin, O. and Henderson, W.A., **2022**. Electrolyte Solvation and Ionic Association: Part IX. Structures and Raman Spectroscopic Characterization of LiFSI Solvates. *Journal of The Electrochemical Society*, *169*(11), p.110544. <a href="https://doi.org/10.1149/1945-7111/ac9a07">https://doi.org/10.1149/1945-7111/ac9a07</a>.
- **52.** Papke, B.L., Ratner, M.A. and Shriver, D.F., **1981**. Vibrational Spectroscopy and Structure of Polymer Electrolytes, Poly (Ethylene Oxide) Complexes of Alkali Metal Salts. *Journal of Physics and Chemistry of Solids*, *42*(6), pp.493-500. <a href="https://doi.org/10.1016/0022-3697(81)90030-5">https://doi.org/10.1016/0022-3697(81)90030-5</a>.
- **53.** Boschin, A. and Johansson, P., **2015**. Characterization of NaX (X: TFSI, FSI)–PEO Based Solid Polymer Electrolytes for Sodium Batteries. *Electrochimica Acta*, *175*, pp.124-133. https://doi.org/10.1016/j.electacta.2015.03.228.
- **54.** Wang, J., Yamada, Y., Sodeyama, K., Chiang, C.H., Tateyama, Y. and Yamada, A., **2016**. Superconcentrated Electrolytes for a High-Voltage Lithium-Ion battery. *Nature Communications*, *7*(1), p.12032. <a href="https://doi.org/10.1038/ncomms12032">https://doi.org/10.1038/ncomms12032</a>.

- **55.** Zheng, J., Chen, S., Zhao, W., Song, J., Engelhard, M.H. and Zhang, J.G., **2018**. Extremely Stable Sodium Metal Batteries Enabled by Localized High-Concentration Electrolytes. *ACS Energy Letters*, *3*(2), pp.315-321. <a href="https://doi.org/10.1021/acsenergylett.7b01213">https://doi.org/10.1021/acsenergylett.7b01213</a>.
- **56.** Yang, H., Qiao, Y., Chang, Z., Deng, H., He, P. and Zhou, H., **2021**. A Safe and Sustainable Lithium-Ion–Oxygen Battery based on a Low-Cost Dual-Carbon Electrodes Architecture. *Advanced Materials*, *33*(24), p.2100827. https://doi.org/10.1002/adma.202100827.
- **57.** Liu, Q., Yu, T., Yang, H., Xu, S., Li, H., Chen, K., Xu, R., Zhou, T., Sun, Z. and Li, F., **2022**. Ion Coordination to Improve Ionic Conductivity in Polymer Electrolytes for High Performance Solid-State Batteries. *Nano Energy*, *103*, p.107763. <a href="https://doi.org/10.1016/j.nanoen.2022.107763">https://doi.org/10.1016/j.nanoen.2022.107763</a>.
- 58. Yu, J., Ren, W., Yu, C., Wang, Z., Xie, Y. and Qiu, J., 2023. Enhanced Anion-Derived Inorganic-Dominated Solid Electrolyte Interphases for High-Rate and Stable Sodium Storage. *Energy & Environmental Materials*, p.e12602. <a href="https://doi.org/10.1002/eem2.12602">https://doi.org/10.1002/eem2.12602</a>.
- **59.** Wróbel, P., Kubisiak, P. and Eilmes, A., **2021**. NaFSI and NaTFSI Solutions in Ether Solvents from Monoglyme to Poly (Ethylene Oxide)—A Molecular Dynamics Study. *The Journal of Physical Chemistry B*, *125*(36), pp.10293-10303. https://doi.org/10.1021/acs.jpcb.1c05793.
- **60.** Henderson, W.A., Brooks, N.R., Brennessel, W.W. and Young, V.G., **2003**. Triglyme–Li<sup>+</sup> Cation Solvate Structures: Models for Amorphous Concentrated Liquid and Polymer Electrolytes (I). *Chemistry of Materials*, *15*(24), pp.4679-4684. <a href="https://doi.org/10.1021/cm034351z">https://doi.org/10.1021/cm034351z</a>.
- **61.** Henderson, W.A., Brooks, N.R. and Young, V.G., **2003**. Triglyme–Li<sup>+</sup> Cation Solvate Structures: Models for Amorphous Concentrated Liquid and Polymer Electrolytes (II). *Chemistry of Materials*, *15*(24), pp.4685-4690. <a href="https://doi.org/10.1021/cm034352r">https://doi.org/10.1021/cm034352r</a>.
- **62.** Das, D., Chandrasekaran, A., Venkatram, S. and Ramprasad, R., **2018**. Effect of crystallinity on Li Adsorption in Polyethylene Oxide. *Chemistry of Materials*, *30*(24), pp.8804-8810. https://doi.org/10.1021/acs.chemmater.8b03434.
- **63.** Moreno, J.S., Armand, M., Berman, M.B., Greenbaum, S.G., Scrosati, B. and Panero, S., **2014**. Composite PEO<sub>n</sub>: NaTFSI polymer electrolyte: Preparation, Thermal and Electrochemical Characterization. *Journal of Power Sources*, *248*, pp.695-702. <a href="https://doi.org/10.1016/j.jpowsour.2013.09.137">https://doi.org/10.1016/j.jpowsour.2013.09.137</a>.
- **64.** Qi, X., Ma, Q., Liu, L., Hu, Y.S., Li, H., Zhou, Z., Huang, X. and Chen, L., **2016**. Sodium Bis (Fluorosulfonyl) Imide/Poly (Ethylene Oxide) Polymer Electrolytes for Sodium-Ion Batteries. *ChemElectroChem*, *3*(11), pp.1741-1745. <a href="https://doi.org/10.1002/celc.201600221">https://doi.org/10.1002/celc.201600221</a>.
- **65.** Macdonald, J.R., **1953**. Theory of AC Space-Charge Polarization Effects in Photoconductors, Semiconductors, and Electrolytes. *Physical Review*, *92*(1), p.4. <a href="https://doi.org/10.1103/PhysRev.92.4">https://doi.org/10.1103/PhysRev.92.4</a>.
- **66.** Trukhan, E.M., **1963**. Dispersion of the Dielectric Constant of Heterogeneous Systems. *Soviet Physics-Solid State*, *4*(12), pp.2560-2570.
- 67. Sørensen, T.S. and Compañ, V., 1995. Complex Permittivity of a Conducting, Dielectric Layer Containing Arbitrary Binary Nernst–Planck Electrolytes with Applications to Polymer Films and Cellulose Acetate Membranes. *Journal of the Chemical Society, Faraday Transactions*, 91(23), pp.4235-4250. <a href="https://doi.org/10.1039/FT9959104235">https://doi.org/10.1039/FT9959104235</a>.
- **68.** Klein, R.J., Zhang, S., Dou, S., Jones, B.H., Colby, R.H. and Runt, J., **2006**. Modeling Electrode Polarization in Dielectric Spectroscopy: Ion Mobility and Mobile Ion Concentration

- of Single-Ion Polymer Electrolytes. *The Journal of Chemical Physics*, 124(14). <a href="https://doi.org/10.1063/1.2186638">https://doi.org/10.1063/1.2186638</a>.
- **69.** Munar, A., Andrio, A., Iserte, R. and Compañ, V., **2011**. Ionic Conductivity and Diffusion Coefficients of Lithium Salt Polymer Electrolytes Measured with Dielectric Spectroscopy. *Journal of Non-Crystalline Solids*, *357*(16-17), pp.3064-3069. https://doi.org/10.1016/j.jnoncrysol.2011.04.012.
- **70.** Wang, Y., Sun, C.N., Fan, F., Sangoro, J.R., Berman, M.B., Greenbaum, S.G., Zawodzinski, T.A. and Sokolov, A.P., **2013**. Examination of Methods to Determine Free-ion Diffusivity and Number Density from Analysis of Electrode Polarization. *Physical Review E*, *87*(4), p.042308. https://doi.org/10.1103/PhysRevE.87.042308.
- **71.** Wang, Y., Fan, F., Agapov, A.L., Saito, T., Yang, J., Yu, X., Hong, K., Mays, J. and Sokolov, A.P., **2014**. Examination of the Fundamental Relation Between Ionic Transport and Segmental Relaxation in Polymer Electrolytes. *Polymer*, *55*(16), pp.4067-4076. https://doi.org/10.1016/j.polymer.2014.06.085.
- **72.** Gainaru, C., Stacy, E.W., Bocharova, V., Gobet, M., Holt, A.P., Saito, T., Greenbaum, S. and Sokolov, A.P., **2016**. Mechanism of Conductivity Relaxation in Liquid and Polymeric Electrolytes: Direct Link Between Conductivity and Diffusivity. *The Journal of Physical Chemistry B*, *120*(42), pp.11074-11083. <a href="https://doi.org/10.1021/acs.jpcb.6b08567">https://doi.org/10.1021/acs.jpcb.6b08567</a>.
- **73.** Dam, T., Jena, S.S. and Pradhan, D.K., **2018**. Coupled Ion Conduction Mechanism and Dielectric Relaxation Phenomenon in PEO<sub>20</sub>–LiCF<sub>3</sub>SO<sub>3</sub>-based Ion Conducting Polymer Nanocomposite Electrolytes. *The Journal of Physical Chemistry C*, *122*(8), pp.4133-4143. https://doi.org/10.1021/acs.jpcc.7b11112.
- **74.** Chadwick, A.V., Strange, J.H. and Worboys, M.R., **1983**. Ionic Transport in Polyether Electrolytes. *Solid State Ionics*, 9, pp.1155-1160. <a href="https://doi.org/10.1016/0167-2738(83)90145-5">https://doi.org/10.1016/0167-2738(83)90145-5</a>.
- **75.** Boden, N., Leng, S.A. and Ward, I.M., **1991**. Ionic Conductivity and Diffusivity in Polyethylene Oxode/electrolyte Solutions as Models for Polymer Electrolytes. *Solid State Ionics*, *45*(3-4), pp.261-270. <a href="https://doi.org/10.1016/0167-2738(91)90160-D">https://doi.org/10.1016/0167-2738(91)90160-D</a>.
- **76.** Ferry, A., Doeff, M.M. and De Jonghe, L.C., **1998**. Transport Property and Raman Spectroscopic Studies of the Polymer Electrolyte System P(EO)<sub>n</sub>-NaTFSI. *Journal of the Electrochemical Society*, *145*(5), p.1586. <a href="https://doi.org/10.1149/1.1838522">https://doi.org/10.1149/1.1838522</a>.
- 77. Martín Dalmas, J., van Roekeghem, A., Mingo, N. and Mossa, S., 2024. Can Silica Nanoparticles Improve Lithium Transport in Polymer Electrolytes?. *The Journal of Physical Chemistry C.* <a href="https://doi.org/10.1021/acs.jpcc.3c08080">https://doi.org/10.1021/acs.jpcc.3c08080</a>.
- **78.** Okoshi, M., Chou, C.P. and Nakai, H., **2018**. Theoretical Analysis of Carrier Ion Diffusion in Superconcentrated Electrolyte Solutions for Sodium-Ion Batteries. *The Journal of Physical Chemistry B*, *122*(9), pp.2600-2609. <a href="https://doi.org/10.1021/acs.jpcb.7b10589">https://doi.org/10.1021/acs.jpcb.7b10589</a>.
- 79. Yu, Z., Balsara, N.P., Borodin, O., Gewirth, A.A., Hahn, N.T., Maginn, E.J., Persson, K.A., Srinivasan, V., Toney, M.F., Xu, K. and Zavadil, K.R., 2021. Beyond Local Solvation Structure: Nanometric Aggregates in Battery Electrolytes and their Effect on Electrolyte Properties. *ACS*Energy

  Letters, 7(1), pp.461-470. <a href="https://doi.org/10.1021/acsenergylett.1c02391">https://doi.org/10.1021/acsenergylett.1c02391</a>.
- **80.** Jones, S.D., Bamford, J., Fredrickson, G.H. and Segalman, R.A., **2022**. Decoupling Ion Transport and Matrix Dynamics to Make High Performance Solid Polymer Electrolytes. *ACS Polymers Au*, *2*(6), pp.430-448. <a href="https://doi.org/10.1021/acspolymersau.2c00024">https://doi.org/10.1021/acspolymersau.2c00024</a>.

# **Table of Contents (TOC) Graphic**

